Earth Planet. Sci. Lett. 658 (2025) 119305

Contents lists available at ScienceDirect

Earth and Planetary Science Letters

journal homepage: www.elsevier.com/locate/epsl

Untangling the interplay among tectonics, climate, and erosion in the Himalayas using landscape evolution modeling

Yuqiang Li [a], Xiaoping Yuan [a,*], Charles M. Shobe [b,c], Guillaume Dupont-Nivet [d,e], Kai Cao [a]

[a] State Key Laboratory of Geomicrobiology and Environmental Changes, Hubei Key Laboratory of Critical Zone Evolution, School of Earth Sciences, China University of Geosciences, Wuhan, China
[b] Department of Geology and Geography, West Virginia University, Morgantown, WV, USA.
[c] U.S. Forest Service Rocky Mountain Research Station, Fort Collins, CO, USA.
[d] Géosciences Rennes-UMR CNRS 6118, University of Rennes 1, Rennes, France.
[e] Helmholtz Centre Potsdam, German Research Centre for Geosciences (GFZ), Potsdam, Germany.

ARTICLE INFO

Edited by: J.P. Avouac

Keywords:
Mountain growth
Landscape evolution model
Himalayas
Geomorphology
Uplift
Erosion

ABSTRACT

The interplay between tectonic rock uplift and climatically modulated erosion governs landscape evolution and influences how mountain ranges affect climate, biogeochemical cycling, ecology, and biodiversity. The Himalayas, Earth's highest mountain range, have inspired a large body of work suggesting that Himalayan topography is primarily governed by southward-propagating tectonic deformation. Here, we use a new coupled surface process and orographic precipitation model to test this hypothesis, and to assess the extent to which orographic precipitation effects have modulated the influence of tectonics on Himalayan topography since the Neogene (*circa* 23 million years ago). The model is quantitatively constrained by observed topographic profiles, river profiles, precipitation profiles, erosion rates, and thermochronologic ages from eight major rivers. Results indicate that propagating rock uplift allows a maximum "no erosion" elevation of ~20 km, and largely governs the formation of the present-day topography of the Himalayas, with a secondary role played by orographic-rainfall-influenced fluvial processes as suggested by erosion/uplift ratios of 60–70%. Modeled sediment fluxes from the orogen are 30–40 $\times$ 10^6 m^3/yr per 250-km width (i.e., approximately one drainage basin width). Our methods enable the integration of diverse observations to reconstruct how tectonics and climate have interacted to control the topographic evolution of mountain belts, and allow investigation into the long-term influence of important geomorphic process parameters.

1. Introduction

The long-term landscape evolution of mountain ranges affects climate, biogeochemical cycling, ecology, and biodiversity (Galy et al., 2007). Since the foundational research on potential Late Cenozoic uplift of mountain ranges by Molnar and England (1990), there has been a long-term debate about the roles of tectonics and climate in mountain building. Some proposed that tectonics (e.g., mountain resistance and friction on the main thrust) controls mountain height (Dielforder et al., 2020; Lamb, 2006; Wang and He, 1999), while others suggested that climate-modulated surface processes (e.g., fluvial and glacial erosion) limit mountain height (Brozović et al., 1997; Egholm et al., 2009; Whipple et al., 1999). The Himalayas, the highest mountain belt in the world, provide a natural laboratory for assessing how the interactions between tectonics and climate govern mountain belt topography.

It has been hypothesized that the large-scale topographic form of the Himalayas is largely controlled by southward-propagating deformation (Eizenhöfer et al., 2019; Godard et al., 2009; Wolf et al., 2022). Although tectonic processes that build Himalayan topography are widely researched (Gao et al., 2016; Wolf et al., 2022), their interactions with the climatically-modulated fluvial erosion that usually lowers the landscape remain elusive. Studies testing the relative importance of tectonic and climatic factors in controlling Himalayan topography (Adams et al., 2020; Burbank et al., 2003; Godard et al., 2014) have not reached a consistent conclusion, in part due to the inherent temporal and spatial limitations of geomorphological, thermochronological, and other observational data. Burbank et al. (2003) suggested that the geometry of overthrusting dominantly influences exhumation across the

* Corresponding author.
E-mail address: yuanxiaoping@cug.edu.cn (X. Yuan).

https://doi.org/10.1016/j.epsl.2025.119305
Received 23 September 2024; Received in revised form 27 January 2025; Accepted 5 March 2025
Available online 17 March 2025

Himalayas, but that surface processes are sufficient to balance the tectonics, by comparing apatite fission-track ages with meteorological and geomorphological datasets. Godard et al. (2014) proposed that Himalayan denudation is dominated by tectonic processes, and that precipitation plays a second-order role, by comparing ^{10}Be denudation rates with modern precipitation and rock uplift rates. Adams et al. (2020) found that climate, as represented by modern mean annual precipitation, strongly controls fluvial erosion in the Bhutan Himalaya.

Wolf et al. (2022) provided a consensus resolution to this debate by showing that the relative influence of tectonics and surface processes could be predicted by a dimensionless number (called the Beaumont number and encompassing rheology and surface process parameters), and indicated that the Himalaya–Tibet, as a non-steady-state strength-controlled orogen, is dominated by tectonics. This view is consistent with the results of Godard et al. (2009), who interpreted that the coupling between deformation and erosion is the mechanism for building plateau margins, and Eizenhöfer et al. (2019), who suggested that lateral advection over a fixed ramp sets patterns of the river steepness (k_{sn}) in convergent orogens.

Thus, tectonics and climate have varying degrees of control over mountain building, and Himalayan topography is largely dictated by propagating deformation and resulting rock uplift over surface processes. However, to quantitatively test this hypothesis for the evolution of the orogen has remained difficult. First, one would need to obtain quantitative evidence with which to separate the contributions of tectonics and climatically-modulated erosion to modern topography. Second, due to the much-debated climatic influence on exhumation and deformation in the Himalayas (Beaumont et al., 2001; Clift et al., 2008), it is necessary to resolve the potentially strong orographic precipitation effects on erosion which were not considered in past studies.

Here we complement and expand on past studies by developing a new method to quantitatively test the hypothesis that southward-propagating deformation is the dominant control on the topographic form of the Himalayas. We present a new approach to inferring controls on orogenic topography that relies on using geomorphologic and geochronologic data to constrain the best-fit parameter values of a numerical model combining tectonic, landscape evolution, and orographic precipitation processes. We first reconstruct the growth of the Himalayas using numerical landscape evolution modeling, taking into account tectonic uplift and orographic precipitation (Braun and Willett, 2013; Hergarten and Robl, 2022; Yuan et al., 2019). To determine best-fit models, we compare modeled river profiles, topographic profiles, precipitation profiles, erosion rates, and thermochronologic ages to observations from eight rivers in the Himalayas across ~1500 km. We then use the best-fit models to assess the influence of southward-propagating deformation, fluvial erosion enhanced by orographic precipitation, and other processes in controlling the topographic form of the Himalayas.

2. Materials and methods

2.1. Geological background, propagating uplift, and monsoon precipitation of the Himalayas

The India-Eurasia collision led to crustal accretion and the propagation of a fold-thrust belt responsible for the crustal shortening and rock uplift of the Himalayas (Li et al., 2015) (Figs. 1 and S1; Table S1), well documented and dated by field investigations (DeCelles et al., 2001; Yin, 2006) and validated by numerical experiments (Wolf et al., 2022). Although the India-Eurasia collision started early in the Paleogene (~50 Ma) (van Hinsbergen et al., 2012), thermochronologic ages (Table S1) and stratigraphic and provenance studies suggest that rapid rock uplift and exhumation in the Himalayas began in the early Neogene (~23 Ma) (Clift et al., 2008; Yin, 2006). This is supported by paleoelevation studies in the Himalayas, indicating rapid rise from ~24–21 Ma (Ding et al., 2017; Ibarra et al., 2023). The proto-Himalayan uplift history before 23 Ma is poorly constrained with suggestions of lower elevations of 2–3 km (Ding et al., 2017; Molnar and Stock, 2009), due to the earlier slow rising before widening outward (Wolf et al., 2022). We thus derive an initial, simple uplift function for the proto-Himalayas from 50 Ma to 23 Ma, which ensures a successive transition from vertical uplift to widening of topography at 23 Ma (see Appendix A.3).

The Himalayan tectonic sequence of southward propagation over the past 23 Ma is well established by thermo-kinematic modeling (McQuarrie and Ehlers, 2017; Wolf et al., 2022). This trend is recorded in mountain ranges and foreland basins by stratigraphic, sedimentological, provenance, and thermochronological data (Li et al., 2015). Geophysical observations from GPS, leveling, InSAR, and microseismicity data indicate that rock uplift reaches a maximum at the Himalayan front, but decreases towards the northern plateau and the southern foreland (Feldl and Bilham, 2006). Southward propagation of rock uplift is also shown by spatial patterns in the discharge-adjusted river channel steepness index k_{snQ}, a proxy for rock uplift rate (Adams et al., 2020), showing an asymmetric peak with rapidly southward-decreasing values downstream from the Himalayan front towards the foreland (Fig. 1B).

Due to the rise of the Himalayas since the Paleogene (~50 Ma), warm moist air over the Indian Plate is insulated by these mountains and produces a strong South Asian monsoon (Ding et al., 2017) (Fig. 1). Since the Neogene (~23 Ma), following the rapid rise of the Himalayan topography, the monsoon has caused high rainfall through orographic precipitation over the Himalayan front, forming trans-Himalayan rivers that drive significant fluvial erosion (Clift et al., 2008). Modern meteorologic observations show a pronounced precipitation gradient, ranging from 1 to 6 m/yr from south to north (Bookhagen and Burbank, 2010).

2.2. Coupled surface process and orographic precipitation model

We model landscape change in the Himalayas by coupling the linear feedback precipitation model LFPM (Hergarten and Robl, 2022) and the propagating uplift function of plateau growth (Yuan et al., 2021) into the landscape evolution model FastScape (Braun and Willett, 2013; Yuan et al., 2019), thereby simulating the interactions among uplift, precipitation, and erosion which all vary in space and time during landscape evolution (Fig. 1D). FastScape solves for two-dimensional river erosion, sediment deposition, and hillslope diffusion (Appendix A.1). River erosion rate, according to stream power law (SPL), is expressed by a power-law function of the stream slope (S^n), contributing drainage area (A^m) and upstream averaged precipitation ($\overline{P}^m$), and controlled by the erosional efficiency coefficient (K_p) representing mainly lithology. The sediment deposition rate is obtained by an integration of upstream erosion rates, which is controlled by the dimensionless deposition coefficient (G). Hillslope material flux is modeled using a linear diffusion equation in which flux depends on topographic slope and a hillslope diffusion coefficient (K_D).

The propagating uplift function is a smoothed uplift wave evolving in space and time derived from the outward-growth model of assuming a free "no erosion" topography at elevation h_0, a value greater than present-day observed elevation (Appendices A.3 and A.4). The slope of the assumed "no erosion" topography and the derived rock uplift wave are controlled by another parameter: the characteristic width of propagating uplift (W). Given the consistent displacement of the Himalayan faults (Fig. 1C; Table S1) and stable India-Eurasia convergence since ~20 Ma (Molnar and Stock, 2009), we simplify our model by assuming, through our propagating uplift function (Yuan et al., 2021), constant rates of propagation and uplift although some studies have reported phased uplift patterns (McQuarrie and Ehlers, 2017; Wolf et al., 2022). The simplified uplift function mimicking continuous advection generates a spatiotemporally smoothed uplift pattern caused by discontinuous faults, such that the model smooths the distributions of rock uplift and

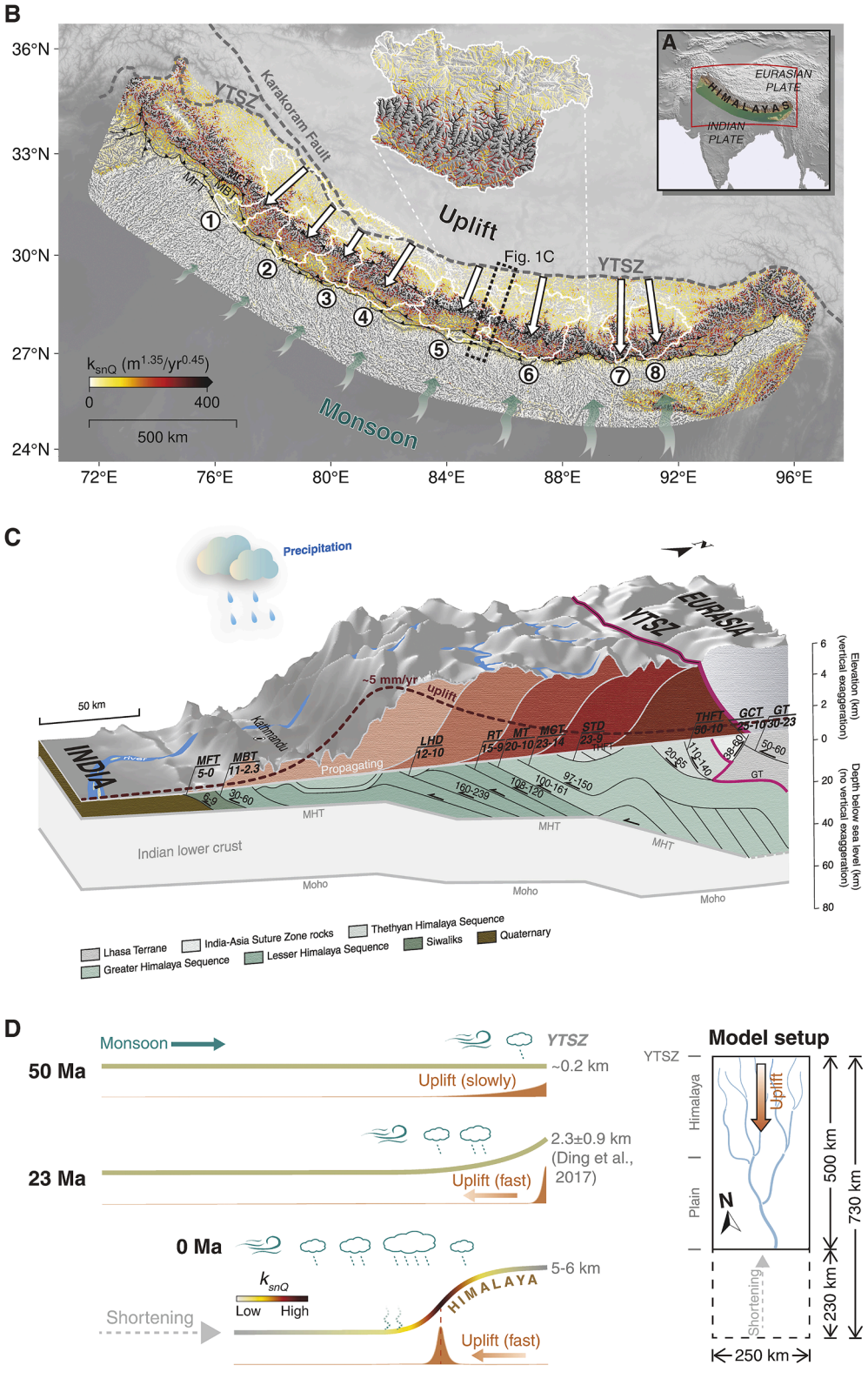

(caption on next page)

Fig. 1. Geological and climatic backgrounds in the Himalayas. (**A**) Location of Fig. 1B in red. (**B**) Topographic map. Over the Himalayas, the river networks are colored by the precipitation-weighted variant of the normalized channel steepness index k_{snQ} (a proxy of uplift rate in the quasi-steady state) (Appendix B). Eight major catchments are outlined with white (see Fig. 2 for their names). White and cyan arrows respectively show uplift propagation and moisture transport (Appendices A.3 and A.4). The major geological structures include the Yarlung–Tsangpo suture zone (YTSZ), the Karakoram fault, the Main Frontal thrust belt (MFT), the Main Boundary thrust belt (MBT), and the Main Central thrust belt (MCT). The black dashed rectangle outlines a zone showing a geological cross section in (C). (**C**) The propagating uplift model and geological structures in the central Himalayas (near Kathmandu, Nepal). The major crust-scale faults, the Main Himalayan Thrust (MHT), and Moho boundary are adapted from seismic reflections (Gao et al., 2016) and geological surveys (Murphy and Yin, 2003). For each of the faults, its name acronym, initiation time (Ma), end time (Ma), slip and displacement (km) are labeled (see more details in Table S1). The geological strata beneath the Himalayas are colored with different green colors from the Lhasa Terrane to the Quaternary basin (Taylor et al., 2021). The dark- to light- red blocks show the southward propagation of the Himalayan topography generally following in sequence thrusting (Li et al., 2015). The brown dashed line shows the present-day vertical velocity fields derived from observations and synthesis of GPS data (Feldl and Bilham, 2006). (**D**) The illustration of two-stage uplift and monsoon precipitation in the Himalayas. The time and space domains are estimated from the references and Google Earth (Appendices A.3 and A.4). The scenario at 0 Ma corresponds to (B). The reference is set at the YTSZ in this study.

erosion. This propagating wave of vertical uplift represents the large-scale variations of deformation over geological time, which is different from the material advection along a fixed crustal ramp assumed in previous models (Coutand et al., 2014; Eizenhöfer et al., 2019).

The orographic precipitation model LFPM adjusts precipitation dynamically in response to topographic change (Appendix A.4). Incoming vapor and cloud water (of total influx F_{in}), driven by wind, undergo advection (controlled by the decay length L_l), dispersion (controlled by the dispersion length L_d), and interaction (i.e., condensation and re-evaporation due to change of topography, controlled by the condensation length L_c). Cloud water ultimately falls as orographic precipitation (controlled by the fallout length L_f).

2.3. Geomorphic and geochronologic analysis of observed and modeled river systems

We chose the eight largest river systems (including trunks and catchments) across the Himalayas based on the following criteria: (1) flowing from the peaks or the interior plateau to the Indus-Ganga foreland, and (2) minimal fault-parallel-flowing sections of trunks (Figs. 1B and 2A). We use the MATLAB-based software TopoToolbox to extract channel profiles as well as maximum and mean swath profiles along the eight river trunks, and transform their horizontal coordinate from distance to upstream integral of drainage area χ (Appendix B) (Fig. 2). The precipitation-weighted variant of the normalized channel steepness index, k_{snQ}, is calculated for all the rivers, including the eight trunks (Appendix B). We also compute broader swath profiles of topography and precipitation, sampled from the area of 500-km length and catchment width (Fig. 3). In addition, we compiled ^{10}Be-derived erosion rates (Codilean et al., 2018) and thermochronological ages (van der Beek and Schildgen, 2023) for the eight studied catchments (Figs. 4 and 5), and verified that general patterns of most cooling ages and erosion rates respond to the orogen-building phase of interest in the modeling rather than to modern active tectonics (see section 3.2).

We model each of the eight river systems separately, considering lateral variations of uplift, precipitation, and lithology across the Himalayas. For each river system, we defined an initial rectangular domain of 730 × 250 km, and assumed an initial topography with random ≤ 200-m elevation noise close to the present-day Indus-Ganga foreland (Fig. 1D). Our models run with initial margin uplift (~0.4 mm/yr) from 50-23 Ma and then propagating uplift (~2 mm/yr) since 23 Ma

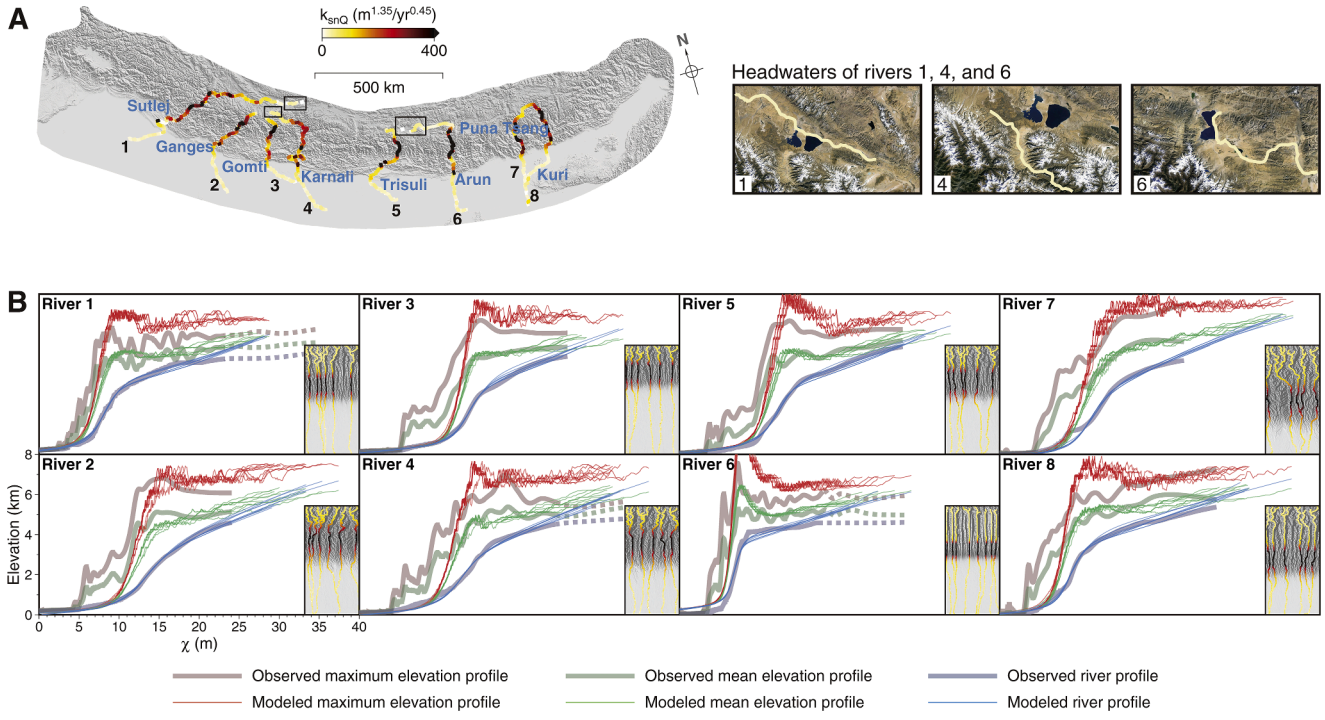

Fig. 2. Comparison of modeled and observed river profiles. (**A**) Map of the eight of the main Himalayan rivers analyzed, colored by k_{snQ}. The headwaters of rivers 1, 4, and 6 connect with the plateau lakes as shown in Google Earth images, so their upstream parts are in the same elevations in χ–elevation plots (the dashed lines in (B)). (**B**) Modeled profiles (thin lines) best fitting the observed profiles (thick lines) for each of the eight rivers (Appendix B). Right-bottom inset on each panel shows modeled topography (the grayed base map) and rivers extracted from 10 headwaters (the lines colored by k_{snQ}).

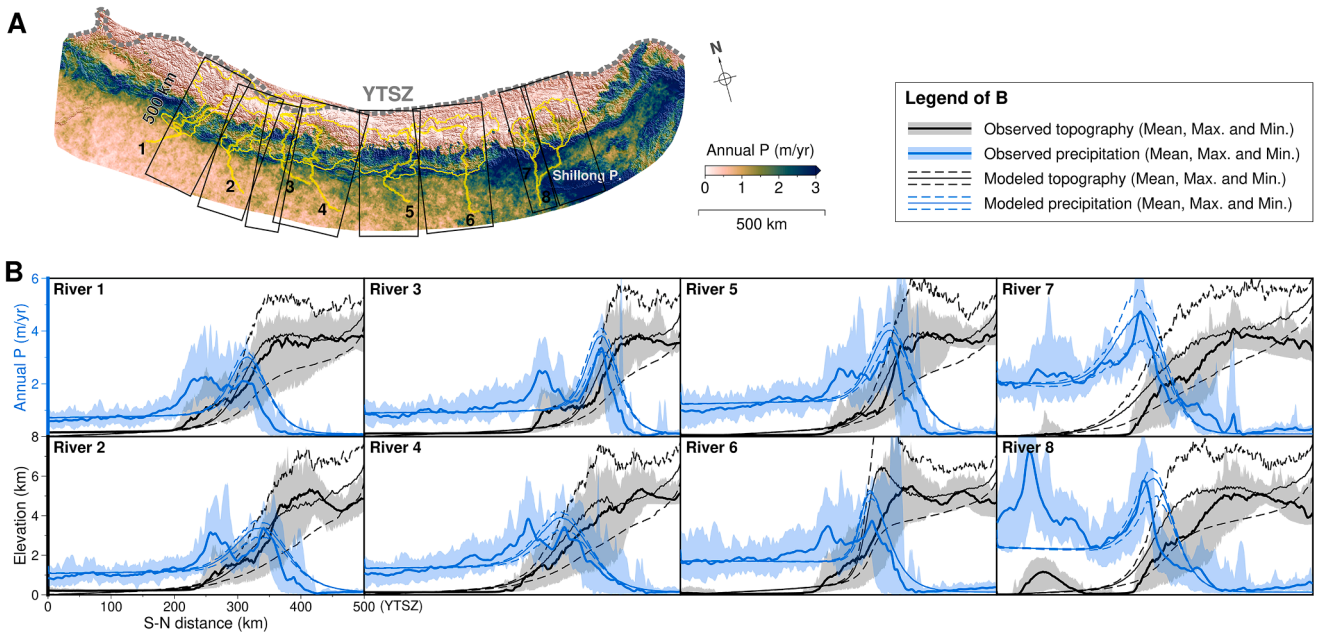

Fig. 3. Comparison of modeled and observed topography and precipitation. (**A**) Map of the Himalayan topography, overlapped with mean annual precipitation (*P*) of 1998 to 2007 (Bookhagen and Burbank, 2010). Eight rivers and corresponding catchments are outlines with yellow. The black boxes show the areas sampled to calculate swath profiles in (B), and on which the following erosion rates (Fig. 4) and cooling ages (Fig. 5) are correspondingly projected. (**B**) Modeled and observed topography and precipitation profiles for each of the eight catchments, according to the legend. YTSZ is the north boundary in (A) and (B).

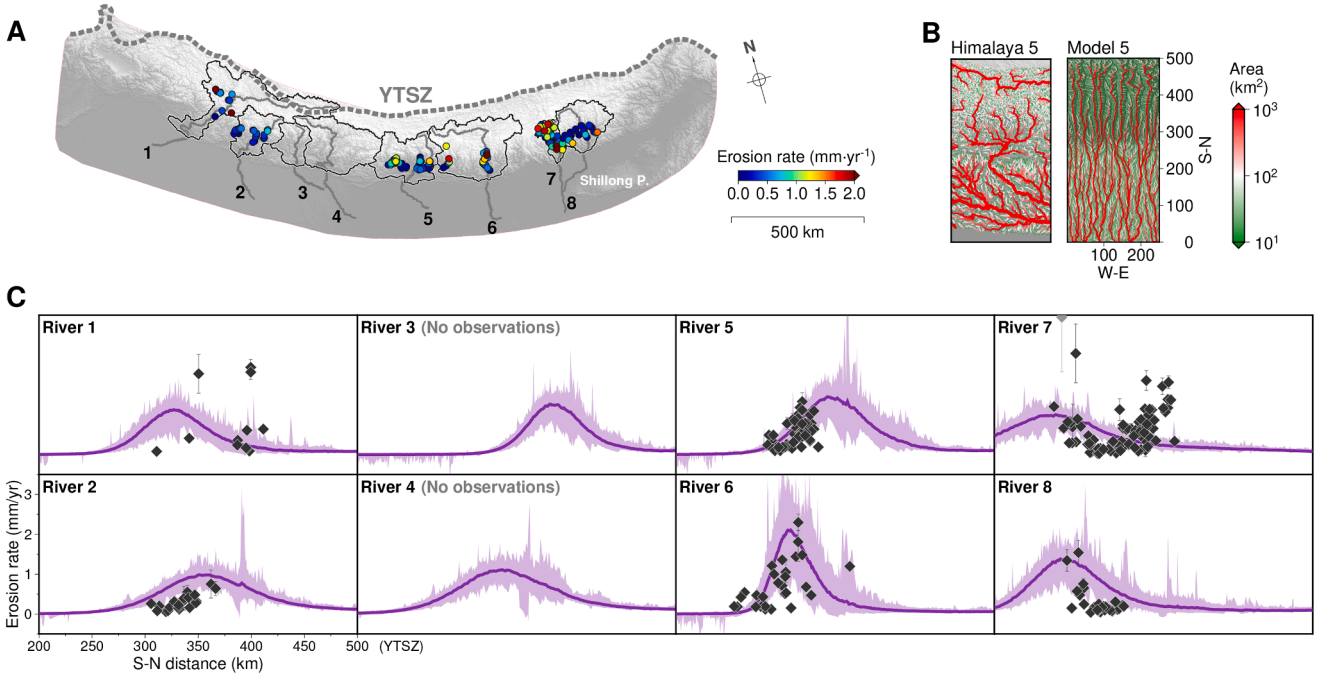

Fig. 4. Comparison of modeled and observed erosion rates. (**A**) ^{10}Be-derived tributary-catchment erosion rates in the Himalayas accessed from the Octopus archive (Codilean et al., 2018). The map shows the (trunk) rivers 1–8 (gray thick lines) and corresponding catchments (black thin lines). (**B**) The stream networks colored by the upstream area in the observed and modeled Himalayas where river 5 drains. (**C**) Modeled and observed short-term erosion rates for each of the eight catchments, projected on the corresponding black box in Fig. 3A. YTSZ is the north boundary in (A) and (C).

(Appendix A.3). A time step length of 10,000 years is used. In each model, we omit belt curvature and assume a uniform horizontal shortening rate of 10 mm/yr since 23 Ma (Appendix A.2), because belt curvature exists at the scale of the entire orogen but is slight for a single 250-km wide catchment (Fig. 1).

At the end of each simulation corresponding to one of the eight river systems, we sample a set of drainage pathways originating from ten headwaters distributed uniformly across the 250-km width and extract channel elevation, maximum and mean elevation, and k_{snQ} values along trunks (Fig. 2B). Swath profiles for topography and precipitation are sampled from the entire model domain (i.e., 500 × 250 km at 0 Ma) (Fig. 3B). We extract modeled tributary-catchment erosion rates over the last time step (i.e., 10 kyr) (Fig. 4C). ^{10}Be-derived erosion rates are averaged over millennial time scales (Godard et al., 2014), and our

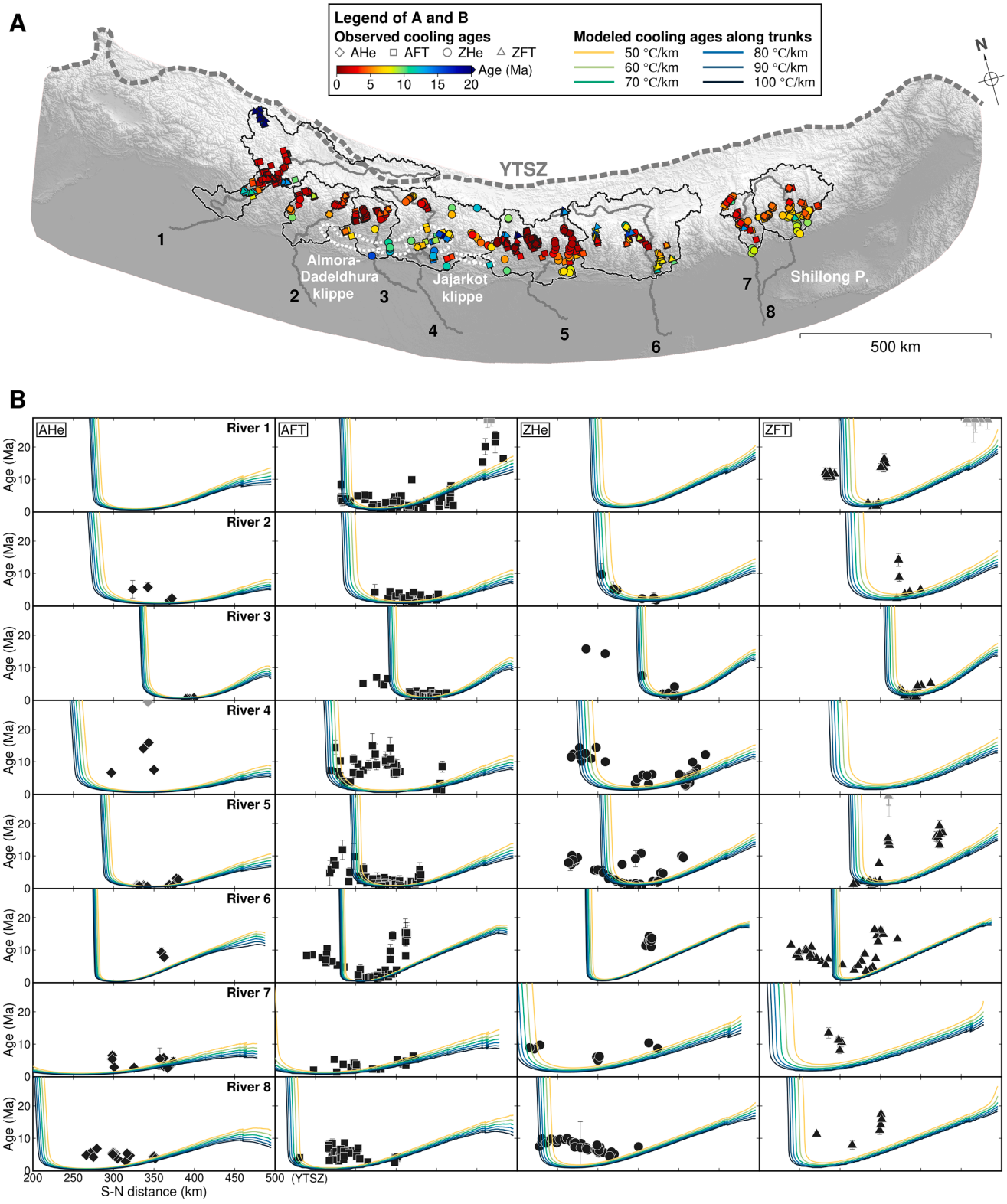

Fig. 5. Comparison of modeled and observed thermochronologic ages. (**A**) Compilation of thermochronologic ages in the eight Himalayan catchments (van der Beek and Schildgen, 2023). Different thermochronometric systems including Apatite (U-Th)/He (AHe), Apatite fission track (AFT), Zircon (U-Th)/He (ZHe), and Zircon fission track (ZFT) are represented by diamond, square, circle, and triangle, respectively, which are all colored by cooling ages. The eight rivers (gray) with corresponding catchments (black) are shown. (**B**) Modeled and observed thermochronologic ages for each of the eight catchments, projected on the corresponding black box in Fig. 3A, according to the legend. YTSZ is the north boundary in (A) and (B).

modeled results are not obviously sensitive to the model time step, such that we can compare modeled versus measured erosion rates. Here, the tributaries are defined to be the cells with drainage area less than 100 km^2, similar to the observed tributary basins (Fig. 4B). The low-temperature thermochronometric ages along the extracted trunks can be predicted from the modeled 50-Myr erosion history using a 1D heat diffusion and advection model (Braun et al., 2006) (Fig. 5B). The observed near-surface geothermal gradients in the Himalayas is from ~50 to ~100 °C/km (Table S2).

2.4. Constraints on model parameters

In this study, we take into account the lateral variations of uplift (i.e., propagating distance, "no erosion" elevation h_0, and characteristic width W), precipitation (i.e., total incoming moisture influx F_{in}, condensation length L_c, fallout length L_f, and decay length L_l), and rock erosional efficiency K_p from the west to east Himalayas (Appendix A). We estimate their best-fit values by comparing the modeled and observed river, topography, and precipitation profiles, because these profiles have different sensitivities to each parameter as indicated by our previous study (Li and Yuan, 2024). Quantitative comparisons between modeled and measured short-term erosion rates and long-term cooling ages give additional constraints on the model parameters. The rock uplift and erosion that occurred in each region over the 50-Myr simulation time represent the relative contributions of tectonics and climatically-driven river erosion to Himalayan topography, and can be quantified by comparing the "no erosion" and "erosion" scenarios of the optimal model.

The main group of models uses the simplest settings of the linear SPL (i.e., $m/n = 0.45/1$) with sediment deposition (i.e., $G = 1$) (Table 1) to simulate landscape evolution, driven by two-stage uplift and orographic precipitation (Fig. S3; Movie S1). In addition, we carry out a sensitivity analysis to study the influences of various conditions, including the classical stream power model (SPL) (i.e., $m/n = 1/2.2$) with no sediment deposition (i.e., $G = 0$) (Fig. S4), different surface shortening rates (Fig. S5), and superimposed uplift caused by a foreland fold-and-thrust belt (Fig. S6).

3. Results

3.1. Model parameters

The optimal values of all the model parameters for eight river systems are given in Table 1, showing that: (1) The maximum elevation of "no erosion" topography h_0 is large in the central Himalayas but small in the eastern Himalayas, implying more exhumation in the central Himalayas but less exhumation in the eastern Himalayas, consistent with observed cooling ages (van der Beek and Schildgen, 2023); (2) The total moisture influx F_{in} is large in the eastern Himalayas but gradually decreases westward, agreeing with modeled and observed moisture transport as well as monsoon precipitation trends over geological time (Bookhagen and Burbank, 2010; Sarr et al., 2022); (3) The erosional efficiency K_p remains relatively consistent among the eight river systems, potentially reflecting similar material properties (e.g., lithology) from the eastern to western Himalayas.

The erosion efficiency K_p and the uplift rate U (set by the parameter h_0) have competing effects on elevation. By varying the maximum "no erosion" elevation h_0 across a range of 10–30 km and the erosion efficiency K_p across a range of 1.1–5.4 × 10^{-6} $m^{-0.35}/yr^{0.55}$ while simultaneously fitting the river profiles and comparing the erosion proxies (i.e., relief, topography, erosion rate, and cooling age) for the river 5 as a test example, we find a unique best-fit value for h_0 of approximately 20 km (Fig. 6).

The presence or absence of modeled orographic rainfall dramatically influences the estimates of the uplift and erosion amounts implied by the "no erosion" elevation h_0 (Fig. 7). The optimal h_0 is estimated to be 20 km for matching the modeled and observed results, using propagating uplift and orographic precipitation in our modeling (Figs. 6 and 7A). The use of uniform precipitation leads to underestimation of h_0 by ~10 km, influencing the resulting uplift and erosion amounts, and causing modeled erosion rates to be too low and cooling ages to be too old (Fig. 7B to D) when comparing to observations. The inclusion of orographic precipitation drives high values of precipitation at the mountain front of ~4 m/yr. Orographically enhanced precipitation can largely unroof the topographic bulge at the Himalayan front, yielding higher erosion rates and lower cooling ages that are better fits to the observations than can be obtained in the uniform precipitation case (Fig. 7A and D). This result highlights that incorporating orographic precipitation is necessary for simulating landscape evolution of

Table 1
The parameters best fitting the multiple observations for each river system in the Himalayas.

Catchment	Landscape evolution model				Propagating uplift function			Orographic precipitation model					
	m*	n*	$G/\bar{p}$†	K_p (m^{1-3m}/yr^{1-m})	Distance (km)	W (km)	h_0 (km)	F_{in} (km^2/yr)	$L_c = L_f$§ (km)	L_l# (km)	L_d** (km)	ϵ_0 (%)	P_b (m/yr)
Range for main models††	0.45	1	1	(1.0–6.0) × 10^{-6}	k_{snQ}§§	10–60	10–30	0.1–2.0	1–100	100–1,000	25	50	0.1
River 1 (i.e., Sutlej)	0.45	1	1	3.0 × 10^{-6}	180	28	15	0.60	20	500	25	50	0.1
River 2 (i.e., Ganges)	0.45	1	1	3.8 × 10^{-6}	150	40	20	0.70	25	500	25	50	0.1
River 3 (i.e., Gomti)	0.45	1	1	3.0 × 10^{-6}	120	24	20	0.78	16	500	25	50	0.1
River 4 (i.e., Karnali)	0.45	1	1	4.0 × 10^{-6}	170	40	20	0.80	25	450	25	50	0.1
River 5 (i.e., Trisuli)	0.45	1	1	3.3 × 10^{-6}	160	28	20	1.00	25	450	25	50	0.1
River 6 (i.e., Arun)	0.45	1	1	2.6 × 10^{-6}	200	14	15	0.80	25	350	25	50	0.1
River 7 (i.e., Puna Tsang)	0.45	1	1	3.6 × 10^{-6}	250	45	15	1.15	16	300	25	50	0.1
River 8 (i.e., Kuri)	0.45	1	1	3.4 × 10^{-6}	240	30	15	1.00	20	300	25	50	0.1

* m/n in stream power law (SPL) is fixed to be 0.45 for the Himalayas (Adams et al., 2020; Olen et al., 2015; Wobus et al., 2006), and n is suggested to 1 in the Siwalik Hills, Nepal (Wobus et al., 2006).

† $G/\bar{p}$ controlling sediment deposition is usually close to 1 when considering precipitation, estimated from experimental and natural landscapes (Guerit et al., 2019).

§ L_c and L_f are usually assumed to be equal suggested by Hergarten and Robl (2022); Smith and Barstad (2004), which are usually 25 km in the modern Himalayas (Hergarten and Robl, 2022).

L_l is about 500 km in the modern Himalayas (Hergarten and Robl, 2022).

** L_d is usually 25 km in the modern Himalayas (Hergarten and Robl, 2022).

†† This table only list tested ranges of parameters for all main models in main text, not including the supplementary models.

§§ Propagating distance of uplift wave refers to the spatial distribution of k_{snQ}, detailed in Fig. 1B and Appendix B.

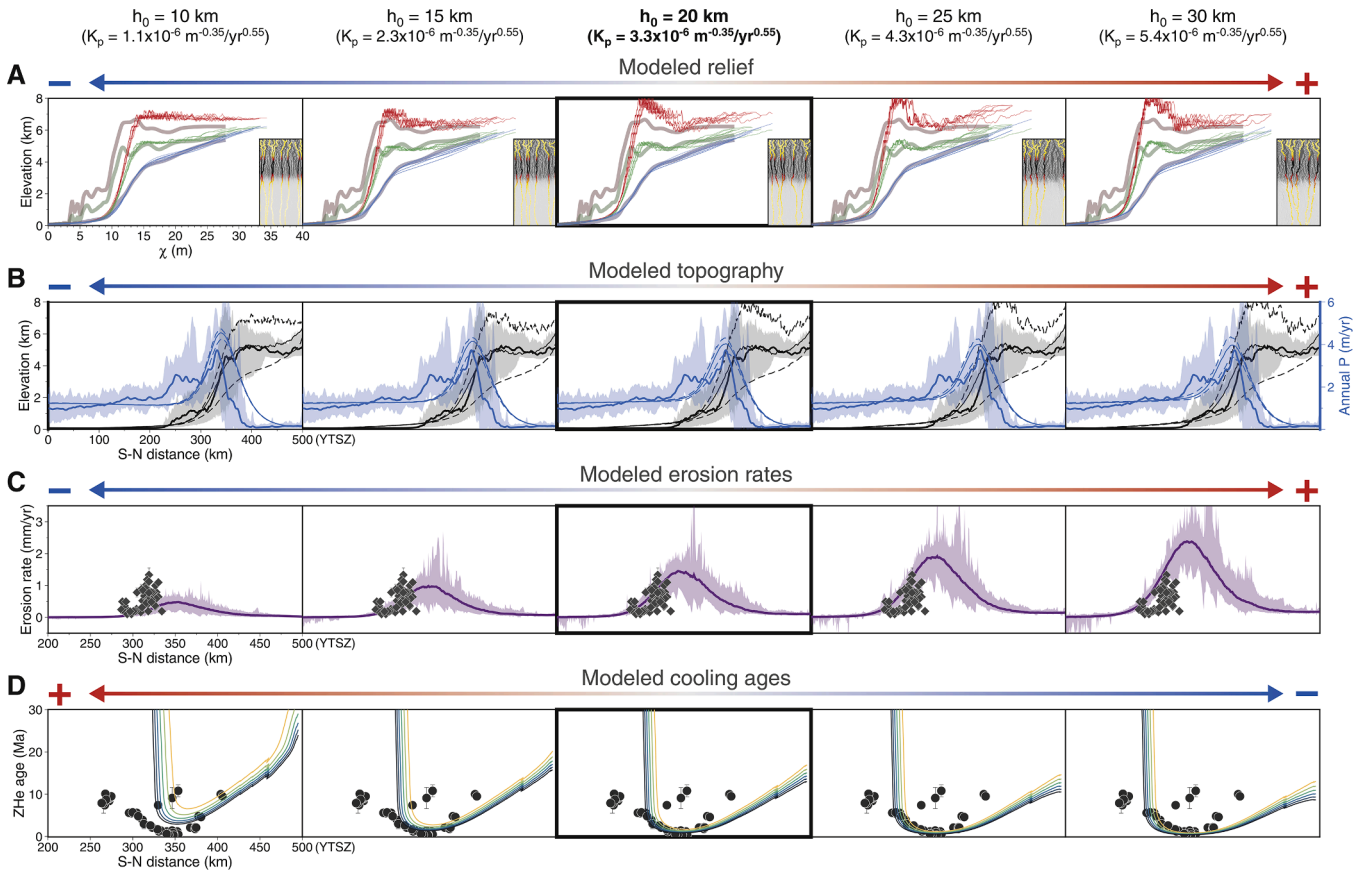

Fig. 6. The different "no erosion" height h_0 and corresponding modeled results for river 5 as a test example. (**A**) Modeled and observed river and elevation profiles, following Fig. 2. (**B**) Modeled and observed topography and precipitation profiles, following Fig. 3. (**C**) Modeled and observed tributary-averaged erosion rates, following Fig. 4. (**D**) Modeled and observed thermochronologic ages, following Fig. 5. Arrows on the upper show the increase (+) and decrease (−) of resulting relief (A), topography (B), erosion rates (C), and cooling ages (D), when fitting the modeled river profiles to the observations in (A) using different "no erosion" height h_0 and erosion efficiency K_p, with the other same parameters in Table 1. The height h_0 = 20 km is most suitable for multiple comparisons and selected as the optimal result for river 5 (thick boxes).

mountain belts and estimating tectonic and climatic effects on topography.

Because we assume uniform erosion efficiency within each of the eight river systems in the Himalayas, our modeling plausibly captures the consistency of erodibility within the main parts of the Himalayas (i.e., the Lesser and Greater Himalayas composed of metamorphic bedrock) but not the Indo-Gangetic foredeep (e.g., the Siwalik Hills which are much lower and are underlain by sediments rather than bedrock). The K_p derived from our main modeling exercise, 2.6−4.0 × 10^{-6}, suggests hard to very hard rocks, compatible with granitic or high-grade metasedimentary rocks (Stock and Montgomery, 1999) and similar to the values fitted by Adams et al. (2020) (~2.5 × 10^{-6} for n = 1). K_p ranges from 10^{-4}–10^{-5} in the Siwalik Hills (Kirby and Whipple, 2001) to 10^{-6} in the Lesser and Greater Himalayas (Adams et al., 2020) for m/n = 0.45 and n = 1, suggesting that our modeling yields estimates of K_p consistent with past work on the Lesser and Greater Himalayas. Although our propagating uplift model is excessively smoothed relative to the real phased uplift pattern caused by a series of faults, the K_p derived from our supplementary modeling with classical SPL (i.e., m/n = 1/2.2 and G = 0) is about 1.4 × 10^{-9} (Fig. S4), comparable to 2.2 × 10^{-9} for n = 2.2 suggested by Adams et al. (2020). Previous studies suggested that there is no substantial difference in the erodibility of different Himalayan rocks or tectonostratigraphic units (Adams et al., 2020; Godard et al., 2014), indicating that our assumption of uniform K_p is reasonable at these scales.

3.2. Multiple comparisons of modeled and observed results

The fit for the eight rivers indicates that the propagating uplift model reasonably replicates the observed river profiles which are convex in their upstream reaches and concave in their downstream reaches, and reproduces appropriately the maximum and mean elevation profiles along the rivers (Fig. 2). The upstream-most reaches of rivers 1, 4 and 6 are not incorporated into the comparison because they extend into plateau lakes at high elevations. The k_{snQ} trends are also similar between the modeled and observed trunks. In addition, our modeling produces 4−6 large rivers per 250 km of orogen width, comparable to one trunk per 50 km in the Himalayas.

Combining propagating uplift and orographic precipitation reproduces topography broadly consistent with the Himalayas consisting of a gentle plateau in the north and steep mountains in the south (Fig. 3). Modeled relief is higher at peaks but lower towards the plateau interior and the foreland, basically consistent with the observed topographic swath profiles. We also find modeled precipitation patterns, in which mean precipitation rates are ~1.0 m/yr in the southern low elevations, abruptly increase to ~4 m/yr in the northern high elevations, and then decrease northward to ~0.2 m/yr, that are consistent with the broad patterns of Himalayan precipitation. An abrupt precipitation peak located at around 100 km in River 8 is caused by the Shillong plateau growing in the front of the eastern Bhutan Himalayas, outside our study area (Fig. 3).

Modeled tributary erosion rates are greatest at the leading edge of the propagating plateau with lower erosion rates in the upstream and

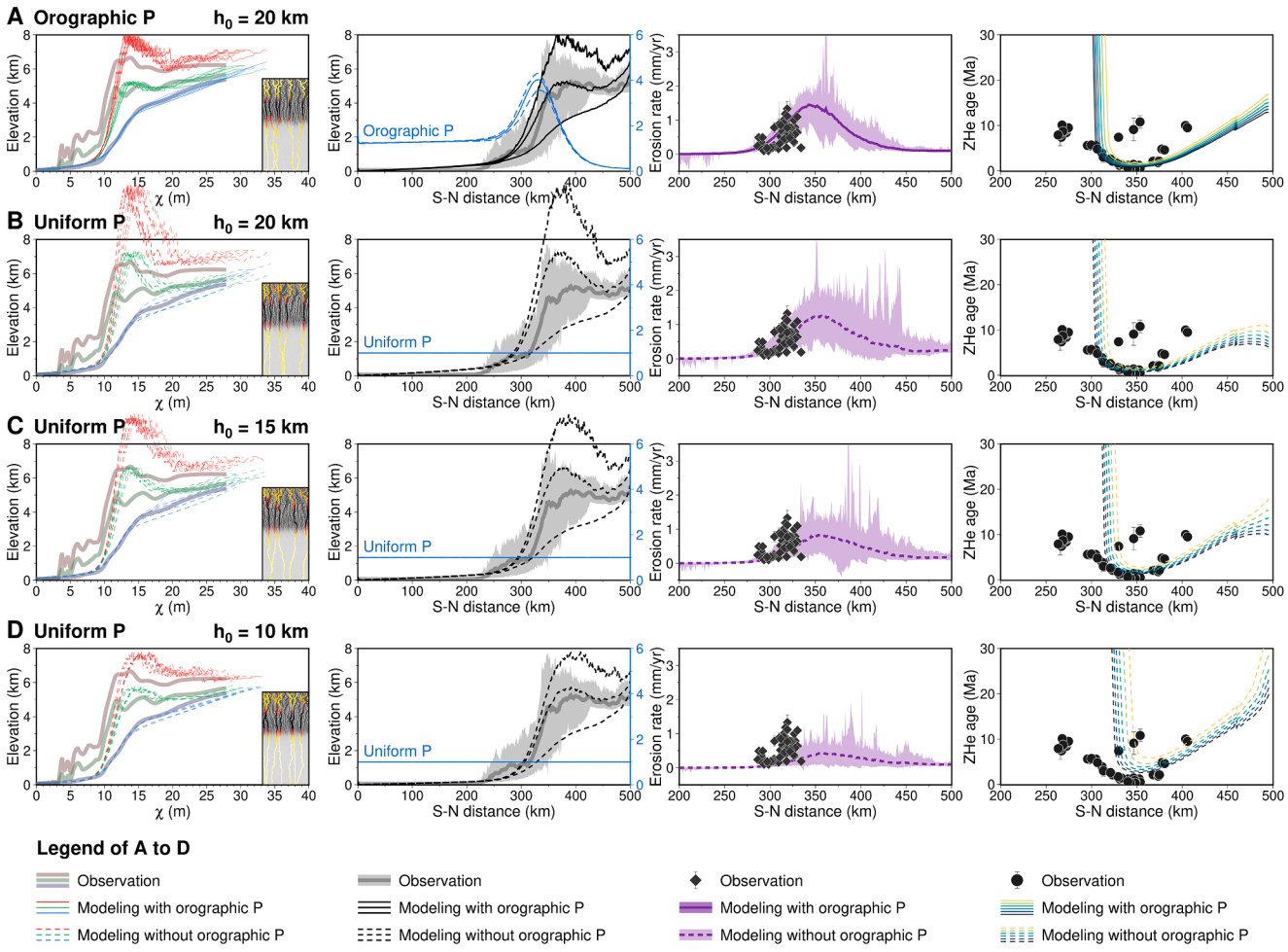

Fig. 7. The modeled results with (**A**) and without (**B** to **D**) orographic precipitation, fitting observed river profiles and comparing other datasets, for river 5 as a test example. Precipitation condition is shown in the second column. h_0 is 20 km and K_p is 3.3×10^{-6} $m^{-0.35}/yr^{0.55}$ in (A); h_0 is 20 km and K_p is 3.0×10^{-6} $m^{-0.35}/yr^{0.55}$ in (B); h_0 is 15 km and K_p is 2.2×10^{-6} $m^{-0.35}/yr^{0.55}$ in (C); h_0 is 10 km and K_p is 1.4×10^{-6} $m^{-0.35}/yr^{0.55}$ in (D). The other parameters, except the precipitation parameters, are the same in the four models (Table 1). The first column: river and elevation profiles, following Fig. 2; the second column: topography swath profiles, following Fig. 3; the third column: tributary-averaged erosion rates, following Fig. 4; the fourth column: thermochronologic ages, following Fig. 5.

downstream areas, consistent with observed ^{10}Be-derived tributary-catchment erosion rates (Fig. 4). Except for a small number of high outliers possibly caused by glaciation in catchments 1 and 7 (Adams et al., 2016; Scherler et al., 2014) and by active faults at the north end of catchment 7 (Le Roux-Mallouf et al., 2015), we find that all erosion rates concentrate in the 0–2.0 mm/yr range and differ among the eight catchments. This is similar to our modeled results (Fig. 4), showing that both observed and modeled erosion rates have different maxima concentrating at different places, e.g., (1) the central Himalayas (rivers 5 and 6) have experienced more rapid erosion, consistent with exhumation rates (van der Beek and Schildgen, 2023) and local relief (Adams et al., 2016); (2) the maximum erosion rates in the eastern Himalayas (rivers 7 and 8) occur further south, consistent with the spatial pattern of k_{snQ} (Fig. 1B).

To validate our best-fit models over million-year timescales, we also compare the modeled and observed ages for different thermochronometric systems (Fig. 5). The general pattern of cooling ages still reflects the million-year exhumation time, although there are frequent earthquakes occurring at local faults. Focusing on the maximum erosion amounts appearing along trunk valleys, we mainly compare our predicted ages along trunk valleys with the lower bound of the observed ages. Modeled and observed ages are roughly comparable in pattern and magnitude; minimum ages of ~1 Ma are found at the leading edge of the propagating plateau, and ages increase gently to the north and increase sharply to the south. Our modeled Himalayan front (i.e., the Greater Himalaya) has a maximum exhumation of ~15 km along the rivers (i.e., 0 Ma in Fig. S3). More exhumation would occur at the modeled Himalayan front (i.e., the Lesser and Greater Himalayas) if we took the foreland thrusts into account (Fig. S6). Given the geothermal gradient of 50–100 °C/km (Table S2), ~15 km exhumation may cause the exposure of high-grade metamorphic rocks (>550 °C) even though we ignore the effect of high pressure in the collision, approaching the metamorphic series (300–700 °C) along the rivers observed in the Himalayas (Beaumont et al., 2001). It should be noted that some of the thermochronometric data come from summits, which usually imply larger ages and thus cannot represent maximum exhumation, e.g., the AFT cooling ages of 10–20 Ma located at around 350 km in catchment 6 (Fig. 5B). In addition, our idealization of a propagating uplift wave ignores some lateral structural variations specific to some Himalayan catchments. The AHe and AFT cooling ages in catchment 4 exceed modeled ages between 300 and 350 km, because the Almora-Dadeldhura klippe located there has formed since 12–14 Ma and uplifted slower than the surrounding area (Sherpa et al., 2022; van der Beek et al., 2016). The AFT and ZHe cooling ages in catchment 8 present are greater (i.e., 5–10 Ma) than modeled between 250 and 300 km because the Shillong Plateau in the front of catchment 8 has accommodated a part of India-Eurasia convergence since 9–14 Ma, reducing uplift and erosion in the eastern Bhutan Himalaya (Coutand et al., 2014).

Our models reproduce the morphologic features of most of the Himalayas, including the Lesser, Greater and Tethyan Himalayas, using the simplified tectonic conditions we impose (Figs. 2 to 5). The only notable misfit corresponds to the foot of the Himalayas, which exhibits local rock uplift near the faults MFT and MBT (Fig. 1A). Seismic tomography and geodynamic modeling suggest a secondary foreland fold-and-thrust belt in front of the strongly-deformed hinterland in the Himalayas (Gao et al., 2016; Wolf et al., 2021). To test the influence of this localized rock uplift, we test an additional model with 0.28 mm/yr of rock uplift between the Lesser Himalaya Duplex (LHD) and the MFT (i.e., from 250 to 350 km along our orogen-perpendicular transect) since 10 Ma, in addition to the main propagating uplift (Fig. S6). This supplementary model produces the missing topography, precipitation, and cooling ages at the foot of the Himalayas. Note that two separate precipitation peaks (e.g., in Rivers 1−6, Fig. 3) are caused by simultaneous activation of one old fault and another renewed fault (e.g., MBT in the foreland) in the Himalayas (Yuan et al., 2024), indicating complexity beyond the simplified foreland uplift (Fig. S6).

Our sensitivity analysis indicates that the uncertainties on the SPL slope exponent n (Fig. S4), sediment deposition coefficient G (Fig. S4), surface shortening rate (Fig. S5), and the superimposed uplift caused by a foreland fold-and-thrust belt (Fig. S6) have no significant influences on uplift and erosion patterns. For the nonlinear and detachment-limited SPL (i.e., $m/n = 1/2.2$ and $G = 0$), there are some trade-offs between n and K_p values (Goren et al., 2014), and between G and K_p values (Yuan et al., 2019, 2021). We compare the modeled and observed erosion rates, as well as other data, so there will be one good case for each set of m/n and G values to fit the observed rates. Our modeling obtains similar results between the case with $m/n = 0.45/1$ and $G = 1$ and the case with $m/n = 1/2.2$ and $G = 0$ (Fig. S4). Due to the increase in the number of model grid cells when increasing the shortening rate from 10 to 20 or 30 mm/yr, the parameters associated with model length (i.e., W, F_{in}, L_l, L_c, and L_f) correspondingly increase. The modeled erosional efficiency K_p is a little larger with higher shortening rates. However, the horizontal shortening rate does not influence the modeled "no erosion" height and the ratio of the eroded to uplifted volumes, which can reflect the relative contributions of tectonics and climate, because the modeling is constrained by observed erosion rates (Fig. S5). The foreland fold-and-thrust belt contributes additional sediment flux out of the Himalayas since ~10 Ma, but this influence is secondary at the scale of the entire Himalayas (Fig. S6).

4. Discussion

4.1. Contributions of propagating rock uplift to Himalayan topography

Our best-fit models with propagating rock uplift since the Miocene (23 Ma), following a slow uplift during the Paleogene (from ~50 Ma to 23 Ma), generate modeled topography consistent with modern observations at the orogen scale. Models can replicate the geomorphological record characterized by elevated and gradually declining k_{snQ} values, tapered topography, and high-relief advection-parallel interfluves (Fig. 2). This supports previous hypotheses that the topographic signature of the tectonic process may be preserved at the locus of active rock uplift in convergent orogens like the Himalayas (Eizenhöfer et al., 2019). Modeled river profiles are consistent with large Himalayan rivers that display convex-up profiles in their upstream reaches and concave-up profiles in their downstream reaches (Fig. 2) (Adams et al., 2016), providing a mechanistic link between the region's propagating rock uplift patterns and channels that deviate from the canonical expectation of generally concave-up rivers (Whipple and Tucker, 1999). Our propagating uplift function with the optimal parameter values (Table 1) results in a smoothed wave-form uplift rate with a maximum of ~2 mm/yr (Fig. S3; Movie S1), which is close to the uplift patterns derived from InSAR, leveling, geomorphologic features, and previous numerical modeling (Feldl and Bilham, 2006). Also, the resulting erosion rates are broadly consistent with ^{10}Be-derived erosion rates in pattern and magnitude (Fig. 4).

Our coupled model of tectonics, landscape evolution, and orographic precipitation, constrained by diverse geomorphic and geologic data, provides a novel line of evidence supporting the hypothesis that a dynamic uplift propagating outward may be primary reason for Himalayan topographic form. Results from data-driven landscape evolution modeling that incorporates orographic precipitation are therefore consistent with geological hypotheses for Li et al. (2015), and numerical modeling of Wolf et al. (2022), the southward propagation of deformation and topography in the Himalayas. Our results also suggest that orographic precipitation strongly influences unroofing. Although our study treats Himalayan tectonics as a boundary condition, previous work has suggested plausible mechanisms of propagation in the Himalayas that would yield a rock uplift pattern consistent with the one we used.

4.2. Quantifying relative contributions of tectonics and climate to the Himalayan landscape

The hypothetical "no erosion" topography at maximum elevation h_0, under only uplift without erosion and deposition (Appendix A.3), reveals the tectonic contribution to mountain building. Our tests with different pairs of h_0 and K_p, fitting river profiles and comparing erosion proxies (i.e., relief, maximum topography, erosion rates, cooling ages), indicate that landscape evolution modeling can uniquely determine the total uplift reflected by h_0 (Fig. 6). Our best-fit h_0 is about 20 km for the central Himalaya (catchment 5, for example), which agrees with ~20-km "no erosion" elevation and ~15-km erosion values derived from balanced cross sections (DeCelles et al., 2001) and thermal-kinematic modeling (Bollinger et al., 2006). Thus, our modeling approach incorporates diverse geomorphic and geochronologic data to quantify tectonic contributions to mountain building that are consistent with those derived from traditional methods.

One key benefit of our modeling approach is the ability to quantify the relative contributions of tectonic uplift and climatically-modulated erosion to landscape evolution by comparing a hypothetical "no erosion" scenario with the best-fit model. We reran our best-fit simulation with zero fluvial erosion efficiency, and compared the topographic difference between the cases without erosion and with erosion using the optimal values of K_p (Figs. 8A and S3); results suggest that the ratio of erosion to uplift amounts falls between 60−70% (Fig. 8B). This proportion of amount lost to erosion relative to the hypothetical no-erosion case is that predicted by minimizing misfit between the modeled and observed river profiles, topographic profiles, precipitation profiles, erosion rates, and thermochronologic ages (Figs. 2 to 7).

We can obtain time-evolving erosion/uplift history in the Himalayas by tracking the sediment flux out of the model domain (of the 250-km model width) from west to east and from Paleogene to Quaternary (Fig. 8C). The evolution of erosion/uplift since Miocene (~23 Ma) shows an increase in the ratio of erosion/uplift amounts through time, because the uplifted rock volume increases rapidly but the remaining rock volume increases slowly. Sediment flux first increases rapidly and then slowly through time, similar to observations of the other drainages originating from the Himalaya-Tibet (Clift, 2006), indicating a gradually stabilizing sediment flux caused by the outward propagation of tectonic deformation and orographic precipitation. The sediment flux from the model domain of 250 × 500 km (i.e., approximately one Himalayan catchment) is estimated to be 30–40 × 10^6 m^3/yr (Fig. 8C), comparable with measurements from Himalayan catchments (Dingle et al., 2016; Lupker et al., 2012). Thus, the modeled total flux from the entire Himalayan front is about 240–320 × 10^6 m^3/yr if we simply assume that the size of the Himalayan Range is ~2000 km (i.e., eight times the model width 250 km), much more than that of all SE and E Asia not including the Himalayas and YTSZ (ca. 60–100 × 10^6 m^3/yr (Clift, 2006)). Our

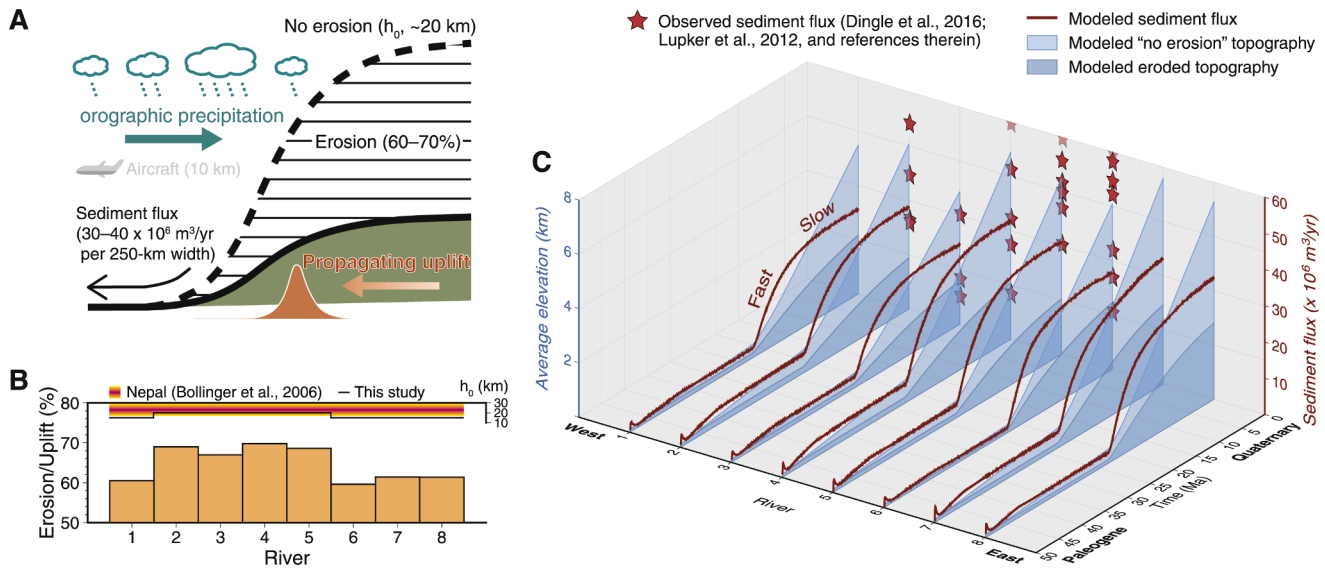

Fig. 8. Amounts of uplift and erosion. (**A**) Illustration of the maximum "no erosion" height h_0, erosion/uplift, and sediment flux in the contexts of propagating uplift and orographic precipitation. (**B**) The ratio of erosion to uplift amounts for eight river systems, derived from the modeled topographies with (i.e., the best-fit values of K_p) and without (i.e., $K_p = 0.00 \times 10^{-6}$ m$^{-0.35}$/yr$^{0.55}$) erosion. The upper (right) y-axis shows the modeled "no erosion" height (h_0) for each river system from west to east Himalayas and the "no erosion" surface elevations in the Nepal Himalaya modeled by Bollinger et al. (2006). (**C**) The average elevations of "no erosion" topographies and eroded topographies, and sediment flux, for eight river systems through time. Our model domain is 250 km wide and 500 km long, including half mountain and half plain, similar to the observed catchment size (Dingle et al., 2016; Lupker et al., 2012) (Fig. 1A).

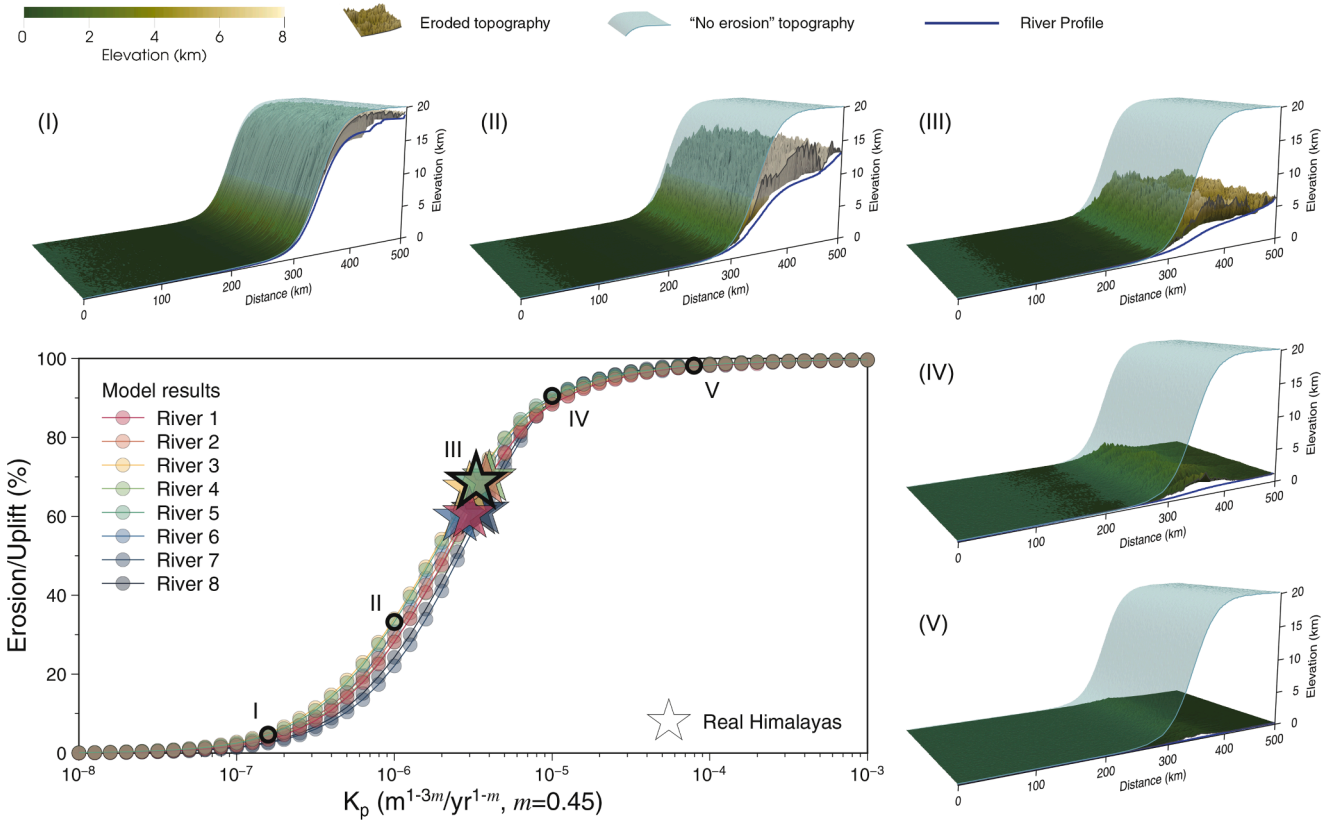

Fig. 9. Relationships between erosion/uplift ratio and erosion efficiency K_p for eight Himalayan river systems. The circles, joined by a curve, represent the modeled results with variable K_p values, and the star represents the result with the optimal K_p value, for each river. The circles and stars thickly outlined are the examples shown in subplots (I)–(V). In each subplot (I)–(V), the surface colored with elevation is the resulting topography with the K_p value in the main figure of Erosion/Uplift–K_p relationships, the surface colored cyan represents the topography with no erosion (i.e., $K_p = 0.00 \times 10^{-6}$ m$^{-0.35}$/yr$^{0.55}$), and the blue curve shows the modeled river profile with the corresponding K_p value.

modeling approach allows reconstruction of the sediment flux out of Himalayas through time, which has important implications for the amount of CO_2 consumed by silicate weathering and thus climate change over geological timescales (Galy et al., 2007).

The supplementary models in which we varied the SPL parameters (Fig. S4), the surface shortening rate (Fig. S5), and the superimposed uplift caused by a foreland fold-and-thrust belt (Fig. S6), show results similar to those from our main model, i.e., "no erosion" height h_0 (20 km), ratio of erosion to uplift amounts (~70%), and sediment flux 30–40 $\times$ 10^6 m^3/yr. We conclude that, due to the dynamics of propagating uplift and orographic precipitation, the Himalayas should be uplifted to ~20-km elevation, and be eroded by 60−70%, which produces a sediment flux of 30–40 $\times$ 10^6 m^3/yr per 250-km width, and that these general results are reasonably insensitive to many details of model setup and parameterization.

4.3. Relationship between erosion/uplift and erosion efficiency in the Himalayas

We study the impact of fluvial erosion efficiency on erosion/uplift assuming a constant uplift function in the sensitivity analysis (Fig. 9). The erosion efficiency K_p encapsulates the resistance of the channel bed to fluvial erosion, is influenced by lithology and other factors (Adams et al., 2020), and is highly variable in nature (Stock and Montgomery, 1999), ranging from 1×10^{-7} to 1×10^{-2} $m^{0.2}$/yr (assuming m/n=0.4). Our modeling results indicate that changes in erosion efficiency can significantly alter the relative contributions of tectonics and climate (Fig. 9). For the Himalayas, erosion/uplift ratios are sensitive to erosion efficiency when the erosion efficiency is between 1×10^{-7} and 1×10^{-5} (m^{1-3m}/yr^{1-m}, m=0.45), but become constant for other values of erosion efficiency.

This idea can be generalized from the Himalayas to orogens globally because the erosion efficiency can control the non-dimensional Beaumont number, Bm, determining types of growing orogens (Wolf et al., 2022; Yuan et al., 2024). We therefore relate the change of material amounts on Earth's surface to the types of orogens determined by theoretical Bm. For example, high mountains (e.g., the Tian Shan and Altai Mountains) or wide plateaus (e.g., the Tibetan Plateau and Central Andes), having Bm greater than 0.5 (Wolf et al., 2022), can form with low erosion efficiency and small erosion/uplift amounts (Fig. 9). In contrast, under high to very high erosion efficiencies, small and narrow mountain belts (e.g., Pyrenees, Taiwan, and Southern Alps of New Zealand), having Bm less than 0.4 (Wolf et al., 2022), will form with large erosion/uplift amounts (Fig. 9). This connection between the rock erosion efficiency, the relative proportions of uplift and erosion, and the shape of mountain ranges expands insight into mountain belt evolution. Under the India-Eurasia collision and the South Asian monsoon (Figs. 1 and S1), the Himalayas are propagating a high-elevation plateau with erosion/uplift ratios of ~70%. When the erosion efficiency is less than 3–4 times current value (i.e., $K_p \leq 1 \times 10^{-5}$ m^{1-3m}/yr^{1-m}, m=0.45), the Himalayas still have a wide plateau (Fig. 9). With much greater values of erosion efficiency, the Himalayas would be a narrow mountain belts and the ratios of erosion/uplift would approach the limit (>90%), similar to the conditions observed in Taiwan and Southern Alps of New Zealand.

Our findings quantitatively show how the form and evolution of the Himalayas reflect the interplay between the primary influence of propagating rock uplift and the secondary influence of orographic precipitation. This result provides new evidence for the hypothesis that the Himalayas is a strength-limited orogen (Wolf et al., 2022). Though we do not incorporate a geodynamic model to assess orogenic strength controls, our propagating rock uplift condition reflects the crust reaching its strength limit because it sets the maximum uplift amount (h_0) and therefore governs the extent of orogenic growth (Wolf et al., 2022). Our landscape evolution modeling study leverages diverse topographic and geochronologic data to relate the amount of material at Earth's surface to the relative influence of tectonics and climate, providing process-based support for existing theoretical hypotheses.

4.4. Model limitations

The model reproduces river profiles, topographic profiles, precipitation profiles, erosion rates, and cooling ages along the eight main rivers across the Himalayas (Figs. 2 to 5) despite incorporating only tectonic uplift, fluvial processes, and hillslope diffusion. Neither glacial nor rockslide erosion is included in our model because they are limited to the high peaks (Lavé et al., 2023). ^{10}Be concentrations measured in the downstream plain and fan indicate that the erosion rates averaged over each of the upstream Himalayan catchments range from 0.5 to 2.4 mm/yr (average ~1.0 mm/yr) (Lupker et al., 2012), similar to our modeled erosion rates of 0−2 mm/yr (Fig. 4). Our best-fit model likely subsumes the erosive effects of glaciation and rockslides into a slightly higher erosional efficiency than would be the case for a landscape evolving exclusively under fluvial processes. If we were to take glaciation and rockslides into account explicitly in the model, it might lead to slightly greater "no erosion" height h_0, ratio of erosion/uplift amounts, and sediment flux.

A tectonic simplification was made in modeling the north of the South Tibetan detachment (STD), where its activation in the Miocene remains poorly constrained (Fig. 1C). However, the total displacement of the STD (20–65 km) is much less than those of the other thrust faults such as the GCT, THFT, MCT, MBT, and MFT (>100 km) (Fig. 1C; Table S1). The STD is also much shallower than the MCT and other thrust faults (Fig. 1C) (Gao et al., 2016). In addition, the entire Himalayas should be contractional, although the STD is an extensional structure (Gao et al., 2016; Yin, 2006). Thus, simplification of the STD in our uplift function likely did not have a first-order influence on our outcomes.

The organization of river networks is influenced by the other controls not included in our simplified models, especially in river reaches flowing parallel to, rather than perpendicular to, the strike of the Himalayan range (e.g., rivers 1, 4, and 6 in Fig. 2A). Olen et al. (2015) argued that the upper reach of river 6 (i.e., Arun) and its slope-break knickzones correspond to the STD, activated at 23−9 Ma (Fig. 1C). Han et al. (2024) proposed that, for the Arun River, the lateral-flowing reach in the Tethyan Himalaya was captured by the downstream reaches at ~89 thousand years ago. However, Adams et al. (2016) suggested that duplex deformation, rather than river capture, produced the similar knickpoints along river profiles in the Bhutan Himalaya, and blockage of renewed faults can also cause lateral flow of rivers (Wolf et al., 2022; Yuan et al., 2024). Despite simplification of the reorganization of Himalayan drainages, e.g., caused by the STD and capture events, our results suggest that propagating uplift and orographic precipitation can explain the major features of trans-Himalayan river profiles (Fig. 2).

5. Conclusions

This study uses coupled tectonic, landscape evolution, and orographic precipitation modeling, constrained by diverse topographic and geochronologic datasets, to test the hypothesis that propagating rock uplift represents the primary control on Himalayan topography. Within the limitations inherent to our modeling assumptions, our method of constraining a landscape evolution model with readily available datasets allows for rough inference of time-varying quantities such as paleo-altitude and rock uplift and erosion amounts, which are difficult to accurately determine using traditional approaches. Our results provide a new line of evidence supporting the idea that propagating rock uplift sets the broad topographic template of the Himalayas; we also suggest a secondary role for orographic precipitation effects. Propagating uplift could drive ~20-km elevations in the Himalayas, but orographically-influenced precipitation eroded 60−70% of the uplifted material, corresponding to a present-day sediment flux of 30–40 $\times$ 10^6 m^3/yr per 250-km width (i.e., approximately one Himalayan

catchment). Our study provides an inversion method to estimate topographic evolution caused by tectonics and climate, providing a process-based way to assess how mountainous topography reflects tectonic dominance and climatic modulation. Studies using approaches similar to ours could shed new light on the growth of other mountain belts on Earth, and help quantitatively establish links among tectonics, climate, mountain belt topography, and biogeochemical cycling.

Funding sources

X.Y. acknowledges funding from National Natural Science Foundation of China (no. 42272261). G.D.-N. acknowledges funding from ANR grant TIBETOP.

CRediT authorship contribution statement

Yuqiang Li: Writing – review & editing, Writing – original draft, Visualization, Validation, Methodology, Investigation, Formal analysis, Data curation, Conceptualization. **Xiaoping Yuan:** Writing – review & editing, Supervision, Software, Project administration, Methodology, Funding acquisition, Formal analysis, Conceptualization. **Charles M. Shobe:** Writing – review & editing, Validation, Supervision, Investigation, Formal analysis. **Guillaume Dupont-Nivet:** Writing – review & editing, Supervision, Funding acquisition, Formal analysis, Conceptualization. **Kai Cao:** Writing – review & editing, Supervision, Investigation, Formal analysis.

Declaration of competing interest

The authors declare that they have no known competing financial interests or personal relationships that could have appeared to influence the work reported in this paper.

Acknowledgments

We thank two anonymous reviewers for their very constructive reviewing and Editor Jean-Philippe Avouac for editorial handling. The findings and conclusions in this publication are those of the authors and should not be construed to represent any official USDA or U.S. Government determination or policy.

Appendix A. Explanation of coupled surface process and orographic precipitation model

A.1. Landscape evolution model

We model the geomorphic evolution of the Himalayas using the FastScape landscape evolution model which solves the equation governing the long-term tectonic uplift, fluvial erosion and sediment deposition (Braun and Willett, 2013; Yuan et al., 2019) as

$$\frac{\partial h}{\partial t} = U - K_f \tilde{p}^m A^m S^n + \frac{G}{\tilde{p}A}\int_A \left(U - \frac{\partial h}{\partial t}\right) dA, \tag{A.1}$$

where $\partial h/\partial t$ is the change rate of topography (m/yr), U is the uplift rate (m/yr), K_f is the fluvial erosion efficiency related to lithology, vegetation, and referential precipitation rate $P_0 = 1$ m/yr ($m^{1\text{-}2m}$/yr), $\tilde{p}$ is the ratio of upstream averaged precipitation $\overline{P}$ to the referential precipitation P_0 (dimensionless), A is the upstream drainage area (m^2), S is the slope in the steepest-descent drainage direction (dimensionless), m and n are the stream power law (SPL) exponents, and G is a dimensionless lumped deposition coefficient encapsulating sediment concentration ratio in transport and settling velocity of sediment (Yuan et al., 2019). It should be noted that, due to the referential precipitation $P_0 = 1$ m/yr,

$$K_f \tilde{p}^m = K_p {P_0}^m \tilde{p}^m = K_p \overline{P}^m, \tag{A.2}$$

where K_p is a new erosional efficiency coefficient that is independent of precipitation, but still encapsulates a number of factors including lithology, vegetation, and other factors ($m^{1\text{-}3m}/yr^{1\text{-}m}$) (Adams et al., 2020). Here, the upstream averaged precipitation $\overline{P}$ for each cell i is calculated by

$$\overline{P} = \sum_{j=ups(i)} P_j \Delta x \Delta y \Big/ \sum_{j=ups(i)} \Delta x \Delta y, \tag{A.3}$$

where P_j is the precipitation rate in each upstream cell j.

Fluvial erosion leads to the formation of hillslopes along river channels. Hillslope processes are commonly represented by a linear diffusion term (Culling, 1960):

$$\frac{\partial h}{\partial t} = K_D \nabla^2 h, \tag{A.4}$$

where K_D is the hillslope diffusion coefficient (m^2/yr).

Concavity m/n in stream power law (SPL) is suggested to be 0.45 for the Himalayas (Fig. S2) (Adams et al., 2020; Olen et al., 2015; Wobus et al., 2006). Wobus et al. (2006) suggested SPL slope exponent $n = 1$ in the Siwalik Hills, Nepal, according to compiled data of many basins subject to a known but variable forcing. Also, deposition coefficient $G/\tilde{p}$ is widely close to one when $n = 1$, estimated from experimental and natural landscapes when considering precipitation (Guerit et al., 2019). They, therefore, are used in a set of main models for eight river systems in the Himalayas (Table 1). In addition, detachment-limited SPL (i.e., $G = 0$) suggests $n = \sim 2.2$ fitting the channel steepness k_{snQ} and ^{10}Be-derived erosion rates in the Himalayas (Adams et al., 2020). Thus, we supply a test for the classical stream power law (i.e., $m/n = 1/2.2$ and $G/\tilde{p} = 0$). It should be noted that a larger n corresponding to a smaller G agrees with the classicl stream law (Guerit et al., 2019), so it is simplified but reasonable to test with $m/n = 1/2.2$ and $G/\tilde{p} = 0$ (Fig. S4). Finally, the erosion efficiency K_p can uniquely be estimated by simultaneously comparing both river profiles and maximum topographic profiles (Fig. 6; Table 1) (Li and Yuan, 2024). Cosmogenic and thermochronologic data can give more similar constraints on the modeled K_p.

Hillslope diffusion coefficient K_D, ranging from 1×10^{-1} to 1×10^{-4} m^2/yr around the world (Richardson et al., 2019), has no substantial influences on modeled results according to Li and Yuan (2024). Thus, K_D is set to be 1×10^{-2} m^2/yr throughout this study for simplicity.

A.2. Boundary conditions

The south boundary of the model domain is set as the base level, i.e., an open boundary where water and sediment flux can leave the system (Fig. 1D). The other three boundaries are all closed where no flux is allowed to leave. Further, model domain, for each catchment, is determined from Google Earth. At present day (i.e., 0 Ma), the N-S length should be 500 km, representing the distance from the Yarlung–Tsangpo suture zone (YTSZ) to a part of the Indus-Ganga plain, and the W-E width is about 250 km, based on the observed catchment width in the Himalayas on average (Fig. 1, B and D). The upstream parts of the Himalayan rivers are limited by the northern Yarlung–Tsangpo catchments, so the comparisons in topography, river length, and drainage divide location on the upstream will be slightly influenced.

We simplify the geological background, assuming a uniform surface shortening along the Himalayan arc because collision occurs anywhere (Fig. 1). Current Global Positioning System (GPS) data shows that, relative to a stable Eurasia, the southern foot of the Himalayas moves northward at ~33−36 mm/yr, whereas the northern margin, i.e., the YTSZ, moves northwards at ~22−25 mm/yr (Liang et al., 2013). In geological history, the average long-term Indo-Himalayan shortening rates determined by various methods are 14±4 mm/yr (Powers et al., 1998). Balanced cross-sections and river terraces indicate that arc-perpendicular shortening velocity along the Himalayas is about 10 mm/yr on average from south to north since the Holocene (Paul Burgess et al., 2012). Meanwhile, the plate reconstructions have suggested that India's convergence with Eurasia slows and stabilizes since ~20 Ma (Molnar and Stock, 2009; van Hinsbergen et al., 2012), so it can be assumed that the development of the Himalayas was the same at steady state with the constant crustal shortening. Thus, we set the N-S shortening rate perpendicular to the Himalayan arc to 10 mm/yr on average for each river system since 23 Ma, i.e., a shortening distance of 230 km. In addition, the shortening of topography before 23 Ma is not taken into account in this study, because the mountain building and exhumation are relatively weak (Clift et al., 2008; Ding et al., 2022) before "hard" collision (Molnar and Stock, 2009; van Hinsbergen et al., 2012). Thus, the initial N-S length of our model is 730 = 500 + 230 km (Fig. 1D). In addition, considering uncertainty on shortening rate which may be larger in the Himalayas, we supply and compare different models with shortening rate of 10 mm/yr (i.e., our main model), 20 mm/yr, and 30 mm/yr (Fig. S5).

A.3. Propagating uplift function

Inspired by the topographic features around the Himalaya-Tibet-Hengduan region (Clark and Royden, 2000; Yuan et al., 2021), we assume a simplified curved topography only with uplift, termed as the hypothetical "no erosion" topography. According to the outward-growth of the Himalayas described in the main text, this imaged "no erosion" topography also propagates southward in the Himalayas during the fast rise stage (i.e., since the Miocene). Here, the "no erosion" topography should be a final result of all the underground processes, such as faulting, folding, channel flowing, and isostatic rebound, opposite to climatic effects. Thus, the propagating uplift rate derived below is a lumped bedrock uplift rate resulting from multiple tectonic activities.

The elevations h_f of the "no erosion" topography at distances x south of the "no erosion" topography margin, x_0, are well represented by a logistic function as (Yuan et al., 2021):

$$h_f(x) = \frac{h_0}{1 + e^{(x-x_0)/W}}, \tag{A.5}$$

where h_0 is the maximum elevation of the hypothetical "no erosion" topography, and W is the characteristic width (of the propagating uplift wave described below). The "no erosion" topography resulting from the outward-growth of the Himalayas also agrees with the high-elevation, low-relief landscape via duplex deformation in the Bhutan Himalaya (Adams et al., 2016) and the distributed basins in the Himalayan hinterland since the Miocene (Ibarra et al., 2023). Assuming the topography margin propagating southward in time t at velocity v_0, the propagating distance x_0 is

$$x_0 = v_0 t. \tag{A.6}$$

Combining the Eqs. (A.5) and (A.6), the uplift rate U can be obtained from the derivative of the "no erosion" topographic profile with respect to time, given that the morphology of this profile is dominated by tectonic uplift without climatic effects (i.e., fluvial erosion and deposition):

$$U = \frac{h_0 v_0 e^{(x-x_0)/W}}{W[1 + e^{(x-x_0)/W}]^2}. \tag{A.7}$$

From the high precipitation-weighted variant of the normalized channel steepness index k_{snQ} (a proxy for uplift rate) section (Fig. 1B), we can approximate the present propagating margin and the corresponding distance of uplift wave during the fast rise stage (i.e., since 23 Ma) (Table 1). For river 5 with its catchment as an example, the propagating distance of uplift wave is ~160 km at present day (Fig. 1B), but the historical propagating distance should be (500 + 230) × (160/500) = 233.6 km in 23 Myr taking the surface shortening into account. Thus, the propagating velocity of uplift wave v_0 is 233.6 km/23 Myr ≈ 10 mm/yr. Finally, we estimate the optimal values of h_0 and W in Eq. (A.7) by comparing modeled and observed river profiles and swath elevation profiles along the rivers (Fig. 6; Table 1) (Li and Yuan, 2024). Cosmogenic and thermochronologic data can give more similar constraints on the modeled h_0.

According to the plate reconstruction (van Hinsbergen et al., 2012), palaeo-altimetric investigation (Ding et al., 2022), and tectonic-surface process modeling (Wolf et al., 2022), the rise of the Himalayan topography involves basically two stages, i.e., one fast propagating uplift began since Neogene (i.e., from 23 Ma to 0 Ma, as the above), and another relatively slow uplift occurred in Paleogene (i.e., from ~50 Ma to 23 Ma) (Fig. 1D). We do not take into account the detailed thrusting processes occurred around the northern boundary YTSZ (including GT, GCT, and more faults) before Neogene (23 Ma) (Murphy and Yin, 2003), and simplify the proto-Himalayan uplift with limited suggestions of lower elevations of 2−3 km (Ding et al., 2022; Molnar and Stock, 2009). Not taking into account climatic effects, the "no erosion" topography at 23 Ma can be calculated based on Eq. (A.5) with an initial propagating distance $x_0 = 0$ m. Thus, the uplift rate in the slow rise stage (i.e., from ~50 Ma to 23 Ma) is simply derived from the "no erosion" topography divided by the period 27 Myr. Given the suggested low palaeo-topography (Ding et al., 2017; Molnar and Stock, 2009) and modest erosion (Clift, 2006; Clift et al., 2008) before 23 Ma, the simplifying assumption of slow uplift driven by thrusting in the YTSZ between 50 and 23 Ma should have only a minor influence on the total uplift and erosion amounts accumulated from 50 to 0 Ma.

Although the uplift functions for before and after 23 Ma are simplified, our model coupling uplift and precipitation yields the palaeo-elevations close to the measured palaeo-elevations in the Qiabulin area and Liuqu Basin near the YTSZ (Ding et al., 2022; Ibarra et al., 2023), i.e., ~2 km before 23 Ma and 5–6 km after 23 Ma (Fig. S3).

A.4. Orographic precipitation model

The main South Asian monsoon transports a large amount of moisture to the Himalayas, in the forms of vapor and cloud water at a given wind velocity. Each component undergoes advection, dispersion, and interaction (i.e., condensation and re-evaporation due to change of topography) processes, keeping in respective moisture balance. The cloud water will finally transfer to be orographic precipitation. In addition, a fraction of the precipitation will evaporate immediately. The above processes for orographic precipitation are described in the linear feedback precipitation model LFPM (Hergarten and Robl, 2022), as the following:

$$-\frac{\partial F_v}{\partial x}+L_d\frac{\partial^2 F_v}{\partial y^2}-\frac{F_v-\beta F_c}{L_c}+\epsilon\frac{F_c}{L_f}=0, \tag{A.8}$$

$$-\frac{\partial F_c}{\partial x}+L_d\frac{\partial^2 F_c}{\partial y^2}+\frac{F_v-\beta F_c}{L_c}-\frac{F_c}{L_f}=0, \tag{A.9}$$

$$\epsilon=\epsilon_0 e^{-\frac{H}{H_0}}, \tag{A.10}$$

where the subscript v/c means the relation for vapor (v) or cloud water (c), F is the advective flux per unit width (m^2/yr), L_d is the dispersion length (m), L_c is the length scale of condensation (m), L_f is the length scale of fallout (m), and ϵ and ϵ_0 are evapotranspiration rates at any altitude H and a reference altitude H_0 respectively (dimensionless). Note that H also represents the topographic elevation h in Eq. (A.1), but in the unit of grid spacing (i.e., 1 km here), and thus H_0 is usually 1 unit grid spacing for convenience. At the same time, the nondimensional coefficient β that determines the dynamic equilibrium in source interaction is

$$\beta=\beta_0 e^{-\frac{H}{H_0}}, \tag{A.11}$$

$$\beta_0=\left(1-\frac{L_c}{L_l}\right)\left(\frac{L_l}{L_f}-1\right), \tag{A.12}$$

where L_l is the length scale of the decay (m). Finally, the effective precipitation that contributes to runoff is

$$P=(1-\epsilon)\frac{F_c}{L_f}+P_b, \tag{A.13}$$

where P_b is a background precipitation rate including other secondary rainfall contributions by other sources (e.g., local lakes), in addition to the South Asian monsoon moisture (m/yr).

Note that (1) L_c and L_f are usually assumed to be equal suggested by Smith and Barstad (2004) and Hergarten and Robl (2022); (2) the dispersion length L_d is set to be 25 km in all the modeling based on the modern Himalayas (Hergarten and Robl, 2022), and its change does not obviously influence the spatially-continuous mountain belt like the Himalayas (Hergarten and Robl, 2022; Li and Yuan, 2024); (3) the reference evapotranspiration rate ϵ_0 is set to be 50% in all the modeling, which can produce the total evapotranspiration amount close to the observation (Li and Yuan, 2024), because our evapotranspiration mechanism is excessively simplified and evapotranspiration amount is much less than the effective precipitation rate in the Himalayas (Bookhagen and Burbank, 2010; Li and Yuan, 2024); (4) the background precipitation rate P_b is set to be 0.1 m/yr in all the modeling, which is close to observed precipitation rate in the rear of Himalayas and also can produce suitable modeling river profile for the Himalayas (Li and Yuan, 2024); (5) The remaining precipitation parameters (i.e., F_{in}, $L_c=L_f$, and L_l) can uniquely be estimated by comparing the modeled and observed features of precipitation profiles (Table 1) (Li and Yuan, 2024).

The monsoon precipitation is further related to the atmosphere dynamic, especially the moisture and wind direction for our model. The South Asian monsoon significantly intensified during the Middle Miocene (17–12 Ma), while keep advancing northwards from the tropic since the middle Eocene (50–45 Ma) (Sarr et al., 2022; Zuo et al., 2024). Around the Himalayas, the vertical integrated moisture transport is estimated to be 100–200 $kg/m^2/s$ at the late Miocene, while the difference of vertical integrated moisture transport between early and late Miocene is about 50–100 $kg/m^2/s$ due to the uplift of the East African and Middle Eastern topography (Sarr et al., 2022). In this study, we preliminarily assume that the total incoming influx of monsoon moisture F_{in} (km^2/yr), including vapor and cloud water, is temporally constant in each modeling. The more comprehensive model coupling our landscape evolution and ocean-atmosphere dynamics is needed to improve our inversion results.

Appendix B. River morphology analysis

The digital elevation model (DEM), accessed from the National Aeronautics and Space Administration (NASA) Shuttle Radar Topography Mission (SRTM) 3 arc (~90 m) second product, is resampled to 200-m resolution. The mean annual precipitation (P) of 1998 to 2007 is calculated from the Tropical Rainfall Measurement Mission (TRMM) product (Bookhagen and Burbank, 2010).

In this study, we extracted the river networks with drainage area exceeding 10 km^2 in the Himalayas using the MATLAB-based software TopoToolbox (Schwanghart and Scherler, 2014). Next, we compute the precipitation-weighted variant of the normalized channel steepness index (i.e., k_{snQ}) for the Himalayan rivers (Fig. 1B), according to (Adams et al., 2020):

$$k_{snQ}=SQ^{m/n}, \tag{B.1}$$

where Q is discharge ($= A\bar{P}$). In the quasi-equilibrium landscapes with respect to current uplift and climate conditions, here the Himalayas (Adams et al., 2020), k_{snQ} can reflect the current uplift information with small uncertainties caused by nonuniform erosional efficiency (i.e., K_p).

To compare the modeled and observed longitudinal profiles, including the river channels and relief, we also apply the χ-transform to the trunks in observations and modeling (Fig. 2), transforming the horizontal coordinate of longitudinal profile from distance to upstream integral of drainage area χ, according to (Perron and Royden, 2013):

$$\chi(x) = \int_{x_b}^{x} \left(\frac{A_0}{A(x)}\right)^{m/n} dx, \tag{B.2}$$

from the base level x_b to the channel reach x, where A_0 ($= 1\ m^2$) is a reference drainage area. Using TopoToolbox (Schwanghart and Scherler, 2014), we also extract the river profiles, and mean and maximum elevation profiles within 50 km-radius swaths along rivers, based on the observed trunk catchment sizes, for the eight main trans-Himalayan trunks from the DEM. We slightly smooth all the profiles (Schwanghart and Scherler, 2014) to remove unimportant noise.

Because (1) the drainage area is difficult to be accurately found for the reaches in the plain, and (2) the change of profile located in the plain is too small relative to that in the mountain, we focus on comparing the χ-elevation profiles located in mountains. Here we rewrite the Eq. (B.2) as

$$\int_{x_b}^{x} \left(\frac{A_0}{A(x)}\right)^{m/n} dx = \int_{plain} \left(\frac{A_0}{A(x)}\right)^{m/n} dx + \int_{mountain} \left(\frac{A_0}{A(x)}\right)^{m/n} dx, \tag{B.3}$$

where the first term on the right-hand side of Eq. (B.3) represents the integration from the base level x_b to the separation place of plain and mountain, whereas the second term is from the separation place to a point x.

Supplementary materials

Supplementary material associated with this article can be found, in the online version, at doi:10.1016/j.epsl.2025.119305.

Data availability

All data are cited in the article and supplementary material. Numerical models are computed with published methods and codes. The software to model landscape evolution is available on https://fastscape.org/fastscapelib-fortran/ (Braun and Willett, 2013; Yuan et al., 2019). The software to model orographic precipitation is available on http://jura.geologie.uni-freiburg.de/openlem/lfpm.php (Hergarten and Robl, 2022).

References

Adams, B.A., Whipple, K.X., Forte, A.M., Heimsath, A.M., Hodges, K.V., 2020. Climate controls on erosion in tectonically active landscapes. Sci. Adv. 6 (42), eaaz3166. https://doi.org/10.1126/sciadv.aaz3166.

Adams, B.A., Whipple, K.X., Hodges, K.V., Heimsath, A.M., 2016. In situ development of high-elevation, low-relief landscapes via duplex deformation in the Eastern Himalayan hinterland. Bhutan. J. Geophys. Res. Earth Surf. 121 (2), 294–319. https://doi.org/10.1002/2015JF003508.

Beaumont, C., Jamieson, R.A., Nguyen, M.H., Lee, B., 2001. Himalayan tectonics explained by extrusion of a low-viscosity crustal channel coupled to focused surface denudation. Nature 414 (6865), 738–742. https://doi.org/10.1038/414738a.

Bollinger, L., Henry, P., Avouac, J.P., 2006. Mountain building in the Nepal Himalaya: Thermal and kinematic model. Earth Planet. Sci. Lett. 244 (1), 58–71. https://doi.org/10.1016/j.epsl.2006.01.045.

Bookhagen, B., Burbank, D.W., 2010. Toward a complete Himalayan hydrological budget: Spatiotemporal distribution of snowmelt and rainfall and their impact on river discharge. J. Geophys. Res. Earth Surf. 115 (F3). https://doi.org/10.1029/2009JF001426.

Braun, J., van der Beek, P., Batt, G., 2006. Quantitative Thermochronology: Numerical Methods for the Interpretation of Thermochronological Data. Cambridge University Press, Cambridge.

Braun, J., Willett, S.D., 2013. A very efficient O(n), implicit and parallel method to solve the stream power equation governing fluvial incision and landscape evolution. Geomorphology 180-181, 170–179. https://doi.org/10.1016/j.geomorph.2012.10.008.

Brozović, N., Burbank, D.W., Meigs, A.J., 1997. Climatic Limits on Landscape Development in the Northwestern Himalaya. Science 276 (5312), 571–574. https://doi.org/10.1126/science.276.5312.571.

Burbank, D.W., Blythe, A.E., Putkonen, J., Pratt-Sitaula, B., Gabet, E., Oskin, M., Barros, A., Ojha, T.P., 2003. Decoupling of erosion and precipitation in the Himalayas. Nature 426 (6967), 652–655. https://doi.org/10.1038/nature02187.

Clark, M.K., Royden, L.H., 2000. Topographic ooze: Building the eastern margin of Tibet by lower crustal flow. Geology 28 (8), 703–706. https://doi.org/10.1130/0091-7613(2000)28<703:TOBTEM>2.0.CO;2.

Clift, P.D., 2006. Controls on the erosion of Cenozoic Asia and the flux of clastic sediment to the ocean. Earth Planet. Sci. Lett. 241 (3), 571–580. https://doi.org/10.1016/j.epsl.2005.11.028.

Clift, P.D., Hodges, K.V., Heslop, D., Hannigan, R., Van Long, H., Calves, G., 2008. Correlation of Himalayan exhumation rates and Asian monsoon intensity. Nat. Geosci. 1 (12), 875–880. https://doi.org/10.1038/ngeo351.

Codilean, A.T., Munack, H., Cohen, T.J., Saktura, W.M., Gray, A., Mudd, S.M., 2018. OCTOPUS: an open cosmogenic isotope and luminescence database. Earth Syst. Sci. Data 10 (4), 2123–2139. https://doi.org/10.5194/essd-10-2123-2018.

Coutand, I., Whipp Jr, D.M., Grujic, D., Bernet, M., Fellin, M.G., Bookhagen, B., Landry, K.R., Ghalley, S.K., Duncan, C., 2014. Geometry and kinematics of the Main Himalayan Thrust and Neogene crustal exhumation in the Bhutanese Himalaya derived from inversion of multithermochronologic data. J. Geophys. Res. Solid Earth 119 (2), 1446–1481. https://doi.org/10.1002/2013JB010891.

Culling, W.E.H., 1960. Analytical Theory of Erosion. J. Geol. 68 (3), 336–344. https://doi.org/10.1086/626663.

DeCelles, P.G., Robinson, D.M., Quade, J., Ojha, T.P., Garzione, C.N., Copeland, P., Upreti, B.N., 2001. Stratigraphy, structure, and tectonic evolution of the Himalayan fold-thrust belt in western Nepal. Tectonics 20 (4), 487–509. https://doi.org/10.1029/2000TC001226.

Dielforder, A., Hetzel, R., Oncken, O., 2020. Megathrust shear force controls mountain height at convergent plate margins. Nature 582 (7811), 225–229. https://doi.org/10.1038/s41586-020-2340-7.

Ding, L., Kapp, P., Cai, F.L., Garzione, C.N., Xiong, Z.Y., Wang, H.Q., Wang, C., 2022. Timing and mechanisms of Tibetan Plateau uplift. Nat. Rev. Earth Environ. 3 (10), 652–667. https://doi.org/10.1038/s43017-022-00318-4.

Ding, L., Spicer, R.A., Yang, J., Xu, Q., Cai, F., Li, S., Lai, Q., Wang, H., Spicer, T.E.V., Yue, Y., Shukla, A., Srivastava, G., Khan, M.A., Bera, S., Mehrotra, R., 2017. Quantifying the rise of the Himalaya orogen and implications for the South Asian monsoon. Geology 45 (3), 215–218. https://doi.org/10.1130/G38583.1.

Dingle, E.H., Sinclair, H.D., Attal, M., Milodowski, D.T., Singh, V., 2016. Subsidence control on river morphology and grain size in the Ganga Plain. Am. J. Sci. 316 (8), 778. https://doi.org/10.2475/08.2016.03.

Egholm, D.L., Nielsen, S.B., Pedersen, V.K., Lesemann, J.E., 2009. Glacial effects limiting mountain height. Nature 460 (7257), 884–887. https://doi.org/10.1038/nature08263.

Eizenhöfer, P.R., McQuarrie, N., Shelef, E., Ehlers, T.A., 2019. Landscape Response to Lateral Advection in Convergent Orogens Over Geologic Time Scales. J. Geophys. Res. Earth Surf. 124 (8), 2056–2078. https://doi.org/10.1029/2019JF005100.

Feldl, N., Bilham, R., 2006. Great Himalayan earthquakes and the Tibetan plateau. Nature 444 (7116), 165–170. https://doi.org/10.1038/nature05199.

Galy, V., France-Lanord, C., Beyssac, O., Faure, P., Kudrass, H., Palhol, F., 2007. Efficient organic carbon burial in the Bengal fan sustained by the Himalayan erosional system. Nature 450 (7168), 407–410. https://doi.org/10.1038/nature06273.

Gao, R., Lu, Z., Klemperer, S.L., Wang, H., Dong, S., Li, W., Li, H., 2016. Crustal-scale duplexing beneath the Yarlung Zangbo suture in the western Himalaya. Nat. Geosci. 9 (7), 555–560. https://doi.org/10.1038/ngeo2730.

Godard, V., Bourlès, D.L., Spinabella, F., Burbank, D.W., Bookhagen, B., Fisher, G.B., Moulin, A., Léanni, L., 2014. Dominance of tectonics over climate in Himalayan denudation. Geology 42 (3), 243–246. https://doi.org/10.1130/G35342.1.

Godard, V., Cattin, R., Lavé, J., 2009. Erosional control on the dynamics of low-convergence rate continental plateau margins. Geophys. J. Int. 179 (2), 763–777. https://doi.org/10.1111/j.1365-246X.2009.04324.x.

Goren, L., Fox, M., Willett, S.D., 2014. Tectonics from fluvial topography using formal linear inversion: Theory and applications to the Inyo Mountains. California. J. Geophys. Res. Earth Surf. 119 (8), 1651–1681. https://doi.org/10.1002/2014JF003079.

Guerit, L., Yuan, X.-P., Carretier, S., Bonnet, S., Rohais, S., Braun, J., Rouby, D., 2019. Fluvial landscape evolution controlled by the sediment deposition coefficient: Estimation from experimental and natural landscapes. Geology 47 (9), 853–856. https://doi.org/10.1130/G46356.1.

Han, X., Dai, J.-G., Smith, A.G.G., Xu, S.-Y., Liu, B.-R., Wang, C.-S., Fox, M., 2024. Recent uplift of Chomolungma enhanced by river drainage piracy. Nat. Geosci. https://doi.org/10.1038/s41561-024-01535-w.

Hergarten, S., Robl, J., 2022. The linear feedback precipitation model (LFPM 1.0) – a simple and efficient model for orographic precipitation in the context of landform evolution modeling. Geosci. Model Dev. 15 (5), 2063–2084. https://doi.org/10.5194/gmd-15-2063-2022.

Ibarra, D.E., Dai, J., Gao, Y., Lang, X., Duan, P., Gao, Z., Chen, J., Methner, K., Sha, L., Tong, H., Han, X., Zhu, D., Li, Y., Tang, J., Cheng, H., Chamberlain, C.P., Wang, C., 2023. High-elevation Tibetan Plateau before India–Eurasia collision recorded by triple oxygen isotopes. Nat. Geosci. https://doi.org/10.1038/s41561-023-01243-x.

Kirby, E., Whipple, K., 2001. Quantifying differential rock-uplift rates via stream profile analysis. Geology 29 (5), 415–418. https://doi.org/10.1130/0091-7613(2001)029<0415:QDRURV>2.0.CO;2.

Lamb, S., 2006. Shear stresses on megathrusts: Implications for mountain building behind subduction zones. J. Geophys. Res. Solid Earth 111 (B7). https://doi.org/10.1029/2005JB003916.

Lavé, J., Guérin, C., Valla, P.G., Guillou, V., Rigaudier, T., Benedetti, L., France-Lanord, C., Gajurel, A.P., Morin, G., Dumoulin, J.P., Moreau, C., Galy, V., 2023. Medieval demise of a Himalayan giant summit induced by mega-landslide. Nature 619 (7968), 94–101. https://doi.org/10.1038/s41586-023-06040-5.

Le Roux-Mallouf, R., Godard, V., Cattin, R., Ferry, M., Gyeltshen, J., Ritz, J.-F., Drupka, D., Guillou, V., Arnold, M., Aumaître, G., Bourlès, D.L., Keddadouche, K., 2015. Evidence for a wide and gently dipping Main Himalayan Thrust in western Bhutan. Geophys. Res. Lett. 42 (9), 3257–3265. https://doi.org/10.1002/2015GL063767.

Li, Y., Wang, C., Dai, J., Xu, G., Hou, Y., Li, X., 2015. Propagation of the deformation and growth of the Tibetan–Himalayan orogen: A review. Earth Sci. Rev. 143, 36–61. https://doi.org/10.1016/j.earscirev.2015.01.001.

Li, Y., Yuan, X., 2024. Coupled Surface Process and Orographic Precipitation Model for the Landscape Evolution of the Himalayas. J. Earth Sci. 35 (3), 1063–1068. https://doi.org/10.1007/s12583-024-2012-x.

Liang, S., Gan, W., Shen, C., Xiao, G., Liu, J., Chen, W., Ding, X., Zhou, D., 2013. Three-dimensional velocity field of present-day crustal motion of the Tibetan Plateau derived from GPS measurements. J. Geophys. Res. Solid Earth 118 (10), 5722–5732. https://doi.org/10.1002/2013JB010503.

Lupker, M., Blard, P.-H., Lavé, J., France-Lanord, C., Leanni, L., Puchol, N., Charreau, J., Bourlès, D., 2012. 10Be-derived Himalayan denudation rates and sediment budgets in the Ganga basin. Earth Planet. Sci. Lett. 333-334, 146–156. https://doi.org/10.1016/j.epsl.2012.04.020.

McQuarrie, N., Ehlers, T.A., 2017. Techniques for understanding fold-and-thrust belt kinematics and thermal evolution. In: Law, R.D., Thigpen, J.R., Merschat, A.J., Stowell, H.H. (Eds.), Linkages and Feedbacks in Orogenic Systems Vol. 213. Geological Society of America.

Molnar, P., England, P., 1990. Late Cenozoic uplift of mountain ranges and global climate change: chicken or egg? Nature 346 (6279), 29–34. https://doi.org/10.1038/346029a0.

Molnar, P., Stock, J.M., 2009. Slowing of India's convergence with Eurasia since 20 Ma and its implications for Tibetan mantle dynamics. Tectonics 28 (3). https://doi.org/10.1029/2008TC002271.

Murphy, M.A., Yin, A., 2003. Structural evolution and sequence of thrusting in the Tethyan fold-thrust belt and Indus-Yalu suture zone, southwest Tibet. Geol. Soc. Am. Bull. 115 (1), 21–34. https://doi.org/10.1130/0016-7606(2003)115<0021:SEASOT>2.0.CO;2.

Olen, S.M., Bookhagen, B., Hoffmann, B., Sachse, D., Adhikari, D.P., Strecker, M.R., 2015. Understanding erosion rates in the Himalayan orogen: A case study from the Arun Valley. J. Geophys. Res. Earth Surf. 120 (10), 2080–2102. https://doi.org/10.1002/2014JF003410.

Paul Burgess, W., Yin, A., Dubey, C.S., Shen, Z.-K., Kelty, T.K., 2012. Holocene shortening across the Main Frontal Thrust zone in the eastern Himalaya. Earth Planet. Sci. Lett. 357-358, 152–167. https://doi.org/10.1016/j.epsl.2012.09.040.

Perron, J.T., Royden, L., 2013. An integral approach to bedrock river profile analysis. Earth Surf. Process. Landf. 38 (6), 570–576. https://doi.org/10.1002/esp.3302.

Powers, P.M., Lillie, R.J., Yeats, R.S., 1998. Structure and shortening of the Kangra and Dehra Dun reentrants, Sub-Himalaya, India. Geol. Soc. Am. Bull. 110 (8), 1010–1027. https://doi.org/10.1130/0016-7606(1998)110<1010:SASOTK>2.3.CO;2.

Richardson, P.W., Perron, J.T., Schurr, N.D., 2019. Influences of climate and life on hillslope sediment transport. Geology 47 (5), 423–426. https://doi.org/10.1130/G45305.1.

Sarr, A.-C., Donnadieu, Y., Bolton, C.T., Ladant, J.-B., Licht, A., Fluteau, F., Laugié, M., Tardif, D., Dupont-Nivet, G., 2022. Neogene South Asian monsoon rainfall and wind histories diverged due to topographic effects. Nat. Geosci. 15 (4), 314–319. https://doi.org/10.1038/s41561-022-00919-0.

Scherler, D., Bookhagen, B., Strecker, M.R., 2014. Tectonic control on 10Be-derived erosion rates in the Garhwal Himalaya. India. J. Geophys. Res. Earth Surf. 119 (2), 83–105. https://doi.org/10.1002/2013JF002955.

Schwanghart, W., Scherler, D., 2014. Short Communication: TopoToolbox 2 – MATLAB-based software for topographic analysis and modeling in Earth surface sciences. Earth Surf. Dynam. 2 (1), 1–7. https://doi.org/10.5194/esurf-2-1-2014.

Sherpa, T.Z.L., DeCelles, P.G., Carrapa, B., Schoenbohm, L.M., Wolpert, J., 2022. Bhumichula plateau: A remnant high-elevation low-relief surface in the Himalayan thrust belt of western Nepal. Geol. Soc. Am. Bull. 135 (7-8), 2121–2140. https://doi.org/10.1130/B36481.1.

Smith, R.B., Barstad, I., 2004. A Linear Theory of Orographic Precipitation. J. Atmos. Sci. 61 (12), 1377–1391. https://doi.org/10.1175/1520-0469(2004)061<1377:ALTOOP>2.0.CO;2.

Stock, J.D., Montgomery, D.R., 1999. Geologic constraints on bedrock river incision using the stream power law. J. Geophys. Res. Solid Earth 104 (B3), 4983–4993. https://doi.org/10.1029/98JB02139.

Taylor, M., Forte, A., Laskowski, A., Ding, L., 2021. Active uplift of southern Tibet revealed. GSA Today 31 (8), 4–10. https://doi.org/10.1130/GSATG487A.1.

van der Beek, P., Litty, C., Baudin, M., Mercier, J., Robert, X., Hardwick, E., 2016. Contrasting tectonically driven exhumation and incision patterns, western versus central Nepal Himalaya. Geology 44 (4), 327–330. https://doi.org/10.1130/G37579.1.

van der Beek, P., Schildgen, T.F., 2023. Short communication: age2exhume – a MATLAB/Python script to calculate steady-state vertical exhumation rates from thermochronometric ages and application to the Himalaya. Geochronology 5 (1), 35–49. https://doi.org/10.5194/gchron-5-35-2023.

van Hinsbergen, D.J.J., Lippert Peter, C., Dupont-Nivet, G., McQuarrie, N., Doubrovine Pavel, V., Spakman, W., Torsvik Trond, H., 2012. Greater India Basin hypothesis and a two-stage Cenozoic collision between India and Asia. Proc. Natl. Acad. Sci. U.S.A. 109 (20), 7659–7664. https://doi.org/10.1073/pnas.1117262109.

Wang, K., He, J., 1999. Mechanics of low-stress forearcs: Nankai and Cascadia. J. Geophys. Res. Solid Earth 104 (B7), 15191–15205. https://doi.org/10.1029/1999JB900103.

Whipple, K.X., Kirby, E., Brocklehurst, S.H., 1999. Geomorphic limits to climate-induced increases in topographic relief. Nature 401 (6748), 39–43. https://doi.org/10.1038/43375.

Whipple, K.X., Tucker, G.E., 1999. Dynamics of the stream-power river incision model: Implications for height limits of mountain ranges, landscape response timescales, and research needs. J. Geophys. Res. Solid Earth 104 (B8), 17661–17674. https://doi.org/10.1029/1999JB900120.

Wobus, C., Whipple, K.X., Kirby, E., Snyder, N., Johnson, J., Spyropolou, K., Crosby, B., Sheehan, D., 2006. Tectonics from topography: Procedures, promise, and pitfalls. In: Willett, S.D., Hovius, N., Brandon, M.T., Fisher, D.M. (Eds.), Tectonics, Climate, and Landscape Evolution Vol. 398. Geological Society of America, pp. 55–74.

Wolf, S.G., Huismans, R.S., Braun, J., Yuan, X., 2022. Topography of mountain belts controlled by rheology and surface processes. Nature. https://doi.org/10.1038/s41586-022-04700-6.

Wolf, S.G., Huismans, R.S., Muñoz, J.-A., Curry, M.E., van der Beek, P., 2021. Growth of Collisional Orogens From Small and Cold to Large and Hot—Inferences From Geodynamic Models. J. Geophys. Res. Solid Earth 126 (2), e2020JB021168. https://doi.org/10.1029/2020JB021168.

Yin, A., 2006. Cenozoic tectonic evolution of the Himalayan orogen as constrained by along-strike variation of structural geometry, exhumation history, and foreland sedimentation. Earth Sci. Rev. 76 (1), 1–131. https://doi.org/10.1016/j.earscirev.2005.05.004.

Yuan, X., Li, Y., Brune, S., Li, K., Pons, M., Wolf, S.G., 2024. Coordination between deformation, precipitation, and erosion during orogenic growth. Nat. Commun. 15 (1), 10362. https://doi.org/10.1038/s41467-024-54690-4.

Yuan, X.P., Braun, J., Guerit, L., Rouby, D., Cordonnier, G., 2019. A New Efficient Method to Solve the Stream Power Law Model Taking Into Account Sediment Deposition. J. Geophys. Res. Earth Surf. 124 (6), 1346–1365. https://doi.org/10.1029/2018JF004867.

Yuan, X.P., Huppert, K.L., Braun, J., Shen, X., Liu-Zeng, J., Guerit, L., Wolf, S.G., Zhang, J.F., Jolivet, M., 2021. Propagating uplift controls on high-elevation, low-relief landscape formation in the southeast Tibetan Plateau. Geology 50 (1), 60–65. https://doi.org/10.1130/G49022.1.

Zuo, M., Sun, Y., Zhao, Y., Ramstein, G., Ding, L., Zhou, T., 2024. South Asian summer monsoon enhanced by the uplift of the Iranian Plateau in Middle Miocene. Clim. Past 20 (8), 1817–1836. https://doi.org/10.5194/cp-20-1817-2024.